HAWAIIAN WINTER RAINFALL VARIABILITY DURING CENTRAL PACIFIC (CP) AND EASTERN PACIFIC (EP) EL NIÑO EVENTS

A THESIS SUBMITTED TO THE GRADUATE DIVISION OF THE UNIVERSITY OF HAWAI'I AT MĀNOA IN PARTIAL FULFILLMENT OF THE REQUIREMENTS FOR THE DEGREE OF

MASTER OF SCIENCE

IN

ATMOSPHERIC SCIENCES

AUGUST 2017

By

Xiaoyu Bai

Thesis Committee:

Pao-Shin Chu, Chairperson
Jennifer D. Small Griswold
Christina Karamperidou

ACKNOWLEDGMENTS

I would like to express gratitude to Dr. Pao-Shin Chu, who has been my advisor since I started my graduate studies. I would like to thank my committee members Dr. Griswold and Dr. Karamperidou. Dr. Griswold has given me valuable comments and a lot of encouragements. Dr. Karamperidou has been a great source of help and pointed out the right direction for me.

I highly value everything Boyi Lu helped me from running the WRF models to detailed question discussions. I would also like to give a big thanks to Dillon Dodson helping me out with my thesis writing. A huge thank you to Abby G. Frazier and Kevin Kodama who gave so generously of their time, data and reports. I want to thank Robert Ballard for help with the weather charts. I also want to thank Ning Li, Hui Shi, Hanpei Zhang, Kristine Tofte and my family for all their support and help.

ABSTRACT

Historically, Hawaiian winter (December through February) rainfall is known to be drier-than-normal during El Niño events due to the eastward shift in the subtropical jet stream core over the North Pacific and enhanced sinking motion associated with the local Hadley circulation over the central Pacific. Recent studies suggest that El Niño can be broadly separated into two types: (1) Eastern Pacific (EP) El Niño which has its largest sea surface temperature (SST) anomalies centered in the equatorial eastern Pacific, and (2) Central Pacific (CP) El Niño which has its largest SST anomalies centered in the equatorial central Pacific. When considering El Niño events according to these two types, is Hawaiian winter rainfall still drier-than-normal?

This study first compares precipitation records between 1957 to present of 21 stations from Kauai, Oahu, Maui and Hawaii during the two types of El Niño winters. Results show that all stations are wetter during CP winters than EP winters. Comparison between EP, CP winters and climatology shows that during EP El Niño winters the Hawaiian Islands have a drier-than-normal precipitation pattern, while during CP El Niño winters the Hawaiian Islands have a normal precipitation distribution and, for some stations, slightly wetter-than-normal precipitation anomalies. To find the mechanisms behind these rainfall anomalies during CP and EP winters, further analysis is on the subtropical jet stream, horizontal wind field, vertical velocity, outgoing longwave radiation, specific humidity, and moisture transport. Dynamical downscaling using Advanced Research Weather Research and Forecasting (WRF-ARW) model is adopted to show a detailed wind field distribution and rainfall simulation. The Hawaiian Rainfall Atlas, which is a set of high resolution Hawaiian rainfall maps, is also analyzed to show spatial rainfall anomalies during the two types of El Niño.

Although more research needs to be done, the hypothetical contributions to the wetter conditions on the Hawaiian Islands during CP winters as compared to EP winters are: lower level southwesterly wind anomalies, weaker descending motion over the Islands, and positive specific humidity anomalies over the Islands.

TABLE OF CONTENTS

LIST OF TABLES

LIST OF FIGURES

CHAPTER 1
INTRODUCTION

The Hawaiian Islands form an archipelago that extends over a vast area in the central Pacific Ocean. Among 50 states in the U.S., Hawaii is the only one in the tropics and completely surrounded by the ocean. The topographic form of the Hawaiian Islands consists of a series of volcanic cones with Kauai in the west and the Island of Hawaii in the east (figure 1.1). The volcanism is related to the Northwest-Southeast rift zone on the ocean floor extending 1,600 miles northwest from the Hawaiian Islands. The volcanic activities intermittently occurred throughout the Pleistocene and continues today in the caldera of Mauna Loa on Hawaii. The eruptions built large islands with the lava of the volcanoes being mostly basalt. Volcanoes of basalt are characterized as flat ellipsoidal domes. After long-term erosion, the original flatness of the ellipsoids cause long mountain ridges that provide topographic barriers to the trade winds. Kauai, the oldest of the Islands, is the most strongly eroded, as is provided by the evidence of the deeply cut Waimea Canyon in the western half of the island and the broadly eroded valley lands in the eastern half of the island. Hawaii, the youngest one, has two large mountain masses, Mauna Loa and Mauna Kea, both of which are over 13,000 feet above mean sea level and both of which are only slightly eroded. The islands lying between Kauai and Hawaii are intermediate in age and in the amount of erosion. All the islands are bordered by coral reefs and all have coasts that consist, in part, of cliffs. So not only do marine effects and tropical climate play significant roles to the Hawaiian Islands climate, but the Island topography does well.

In the tropical Pacific, the most prominent feature of the large scale circulation is the the trade wind flow. Hawaiian Islands, southwest of the North Pacific subtropical high, are located in the northeast trade wind region which is the most consistent wind field in the world (Wyrtki and Meyers 1976). The dominance of the trade winds and the influence of the terrain make it very rare for completely cloudless skies to occur and make it common for showers to exist due to orographically induced clouds. The climate of Hawaii can be characterized by two seasons: wet and cool (from November to April) and dry and warm (from May to October). Winter time is the Hawaiian raining season. Trade wind-induced orographic rainfall along the windward side of the island chain is the first dominant factor of Hawaiian statewide precipitation (Leopold 1951; Lyons 1982). Trade winds, although dominant, are not the only major dynamic element that plays an important role on Hawaiian rainfall (Chu et al. 1993; Timm and Diaz 2009; O'Connor et al. 2015). Other weather systems

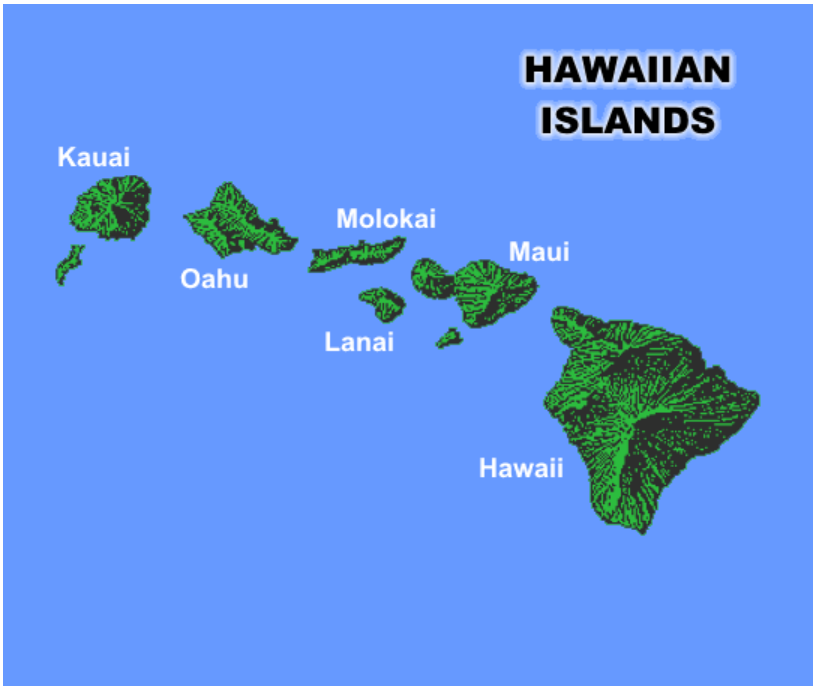

Figure 1.1: Hawaiian Islands. Figure source: ⟨http://www.covingtontravel.com/2016/03/family-friendly-islands-of-hawaii/⟩

that bring rainfall to the Islands include: (1) Cold fronts associated with extratropical storms which bring light to moderate precipitation to the islands especially during the wet season; (2) Kona lows, nonfrontal cutoff low pressure systems lasting for days, leading to the advection of warm and moist southwesterly flows that can form intense rainfall even in dry leeward areas (Morrison and Businger 2001); and (3) Upper level disturbances, sometimes with a closed low pressure center, which occasionally bring abundant rainfall to the Islands. Hurricanes and tropical storms are relatively rare in Hawaii, but if they pass close enough to the Islands they can form heavy rains as well as high winds and waves on the coasts. Unlike Kona lows and cold fronts which are features of the wet season, hurricanes and tropical storms are most likely to be associated with the dry season (July through November).

The rainfall distribution on the Hawaiian Islands is exceedingly uneven. A tremendous amount of rainfall falls in mountainous areas climatologically. However, not all mountain areas are wetter than other areas. Over the Hawaiian Islands, the sinking branch of the Hadley cell sustains a temperature inversion, named the trade wind inversion (TWI), which limits clouds and turbulence like mixing. According to Cao et al. (2007), 80%-90% of the average TWI height is around 2200m. Therefore it is very dry at the top of Hawaii's highest mountains. In addition, thermally-driven local circulation near coasts (for example, land-sea

breezes) and along mountain slopes, and topographic blocking breaks the persistent abundant rainfall pattern along the windward mountain slopes (Diaz and Giambelluca 2012). However, leeward areas and high summits are able to receive significant precipitation when disturbances interrupt TWI.

The economy of the Hawaiian Islands is based firstly on tourism, secondarily on defense and thirdly on agriculture (⟨http://www.newsmax.com/FastFeatures/industries-hawaii-strongest-economy/2015/03/05/id/628087/⟩). The principal agriculture commodity is sugar cane which is a two-year crop with most planted under irrigation. The second most important crop is pineapple, which requires little water and high sunshine. Other agriculture activities include dairying, poultry raising, fruits, nuts, vegetables and coffee raising. Many of these activities have a close relationship to water supply. Therefore research on the Islands rainfall is important to the State of Hawaii.

El Niño-Southern Oscillation (ENSO) is a pseudo-periodical and coupled atmosphere-ocean phenomenon over the tropical eastern Pacific Ocean, affecting much of the tropics and subtropics through teleconnection dynamics. ENSO varies in winds and sea surface temperature (SST) which means that it involves both oceanic and atmospheric interactions. For SST, the phenomenon generally fluctuates between a warmer than average state (El Niño), a cooler than average state (La Niña) and a neutral state. It is also important to know that sub-surface ocean temperature also responds to the ENSO phase. The Southern Oscillation is the atmospheric component of ENSO. The strength of the Southern Oscillation can be shown by the surface air pressure difference between Tahiti (in the Pacific) and Darwin (in Australia, in the Indian Ocean). El Niño is accompanied by lower surface pressure over Tahiti and higher air pressure in Darwin. La Niña, which is the opposite state to El Niño, is accompanied by higher pressure in Tahiti and lower pressure over Darwin.

ENSO, the leading mode of tropical variability, can modulate Hawaii rainfall variability. According to Lyons (1982), during winter time, trade winds and southwest winds explain 71% of the Islands rainfall and during most El Niño winters, Hawaii experiences low trade wind rainfall. Chu (1995) and Chu and Chen (2005) also found that during El Niño winter and spring, droughts tend to occur more often on the Hawaiian Islands. Recent studies show that there is a type of El Niño which is different from the conventional El Niño. That is to say, ENSO has different flavors. According to Ashok et al. (2007); Kao and Yu (2009) and Kug et al. (2009), El Niño events can be broadly characterized by two types: Central Pacific (CP) with its largest SST anomalies centered in the equatorial central Pacific and Eastern Pacific (EP) with its largest SST anomalies centered in the equatorial eastern Pacific. Ashok

et al. (2007) and Lee and McPhaden (2010) also found that CP El Niño events have tended to occur relatively more often than the EP El Niño in recent years. Since the previous works show that the conventional El Niño correlates to a drier Hawaiian winter, would the Hawaiian winter rainfall act differently between CP and EP El Niño winters?

In this study, December through February was defined as the winter period. First, CP and EP events are defined. Precipitation data is then collected from 21 stations located on four main Hawaiian Islands (Kauai, Oahu, Maui and Hawaii) and used to calculate the rainfall difference between CP and EP El Niño winters. Wind direction and wind speed differences between EP and CP winters were analyzed at the 1000 hPa, 850 hPa and 200 hPa levels; vertical velocity, specific humidity, outgoing longwave radiation flux at the top of the atmosphere and SST were also compared to show the large circulation difference between CP and EP El Niño. A nested Advanced Research Weather Research and Forecasting (WRF-ARW) simulation for both CP and EP El Niño winters for Hawaiian Islands was run to show regional variation of the wind field. Hawaiian Rainfall Atlas, which is a set of high resolution maps of the spatial patterns of Hawaiian rainfall, is analyzed for comparison with the station data and the WRF-ARW simulation. The thesis is organized as follows: In chapter 2 and 3, the data and analysis method used to compare the rainfall difference are descried. Model and model physics schemes used to do the Dynamical Downscaling are descried in chapter 4. Chapter 5 presents the results from the analysis. A summary can be found in Chapter 6.

CHAPTER 2
DATA

2.1 Rainfall data

Global Summary of the Month (GSOM) station monthly total precipitation data are obtained from the National Oceanic and Atmospheric Administration (NOAA) / National Centers for Environmental Information (NCEI; Lawrimore (2016) ⟨https://data.noaa.gov/dataset/global-summary-of-the-month-version-1-0⟩) website. From GSOM, 21 stations with the best continuity from the four main Hawaiian Islands are collected. In this study, the time period 1956-2016 is chosen since some of the stations have a large amount of missing values prior to 1956. In addition, several stations on Kauai are excluded due to discontinuous records since the year 2011. The locations of the stations are shown in figure 2.1.

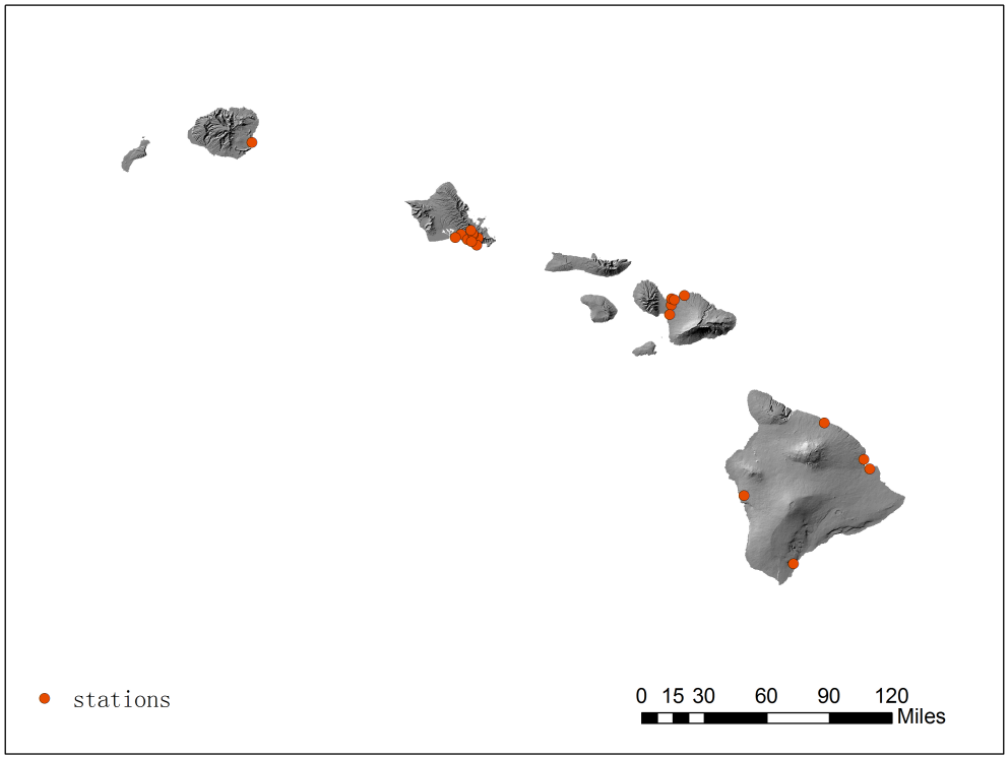

Figure 2.1: Locations of the 21 stations.

2.2 Sea surface temperature (SST) data

NOAA extended reconstructed monthly mean sea surface temperature V4 (ERSSTv4; Huang et al. (2015)) is adopted from NOAA Earth System Research Laboratory (NSRL) Physical Sciences Division (PSD; ⟨https://www.esrl.noaa.gov/psd/data/gridded/data.noaa.ersst.v4.html⟩) website. This data set, ranging from 1854 to the present, has a resolution of 2.0° latitude × 2.0° longitude global grid (89 × 180).

2.3 El Niño index

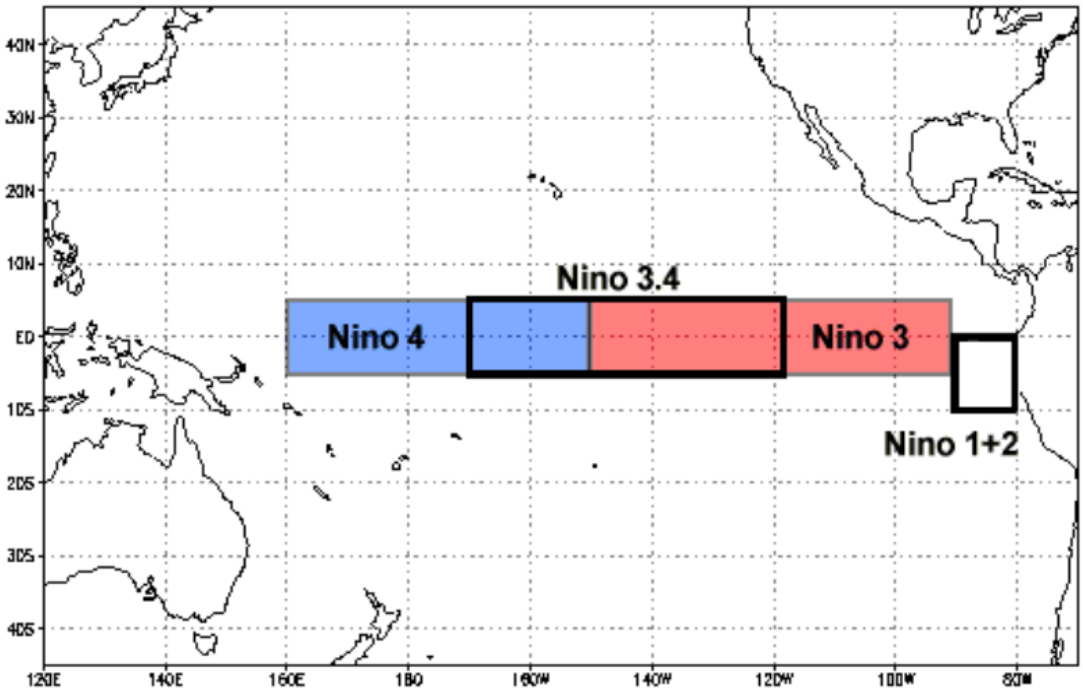

Figure 2.2: Regions of El Niño. Red color indicates Niño 3 region and blue color indicates Niño 4 region. Figure source: ⟨https://www.ncdc.noaa.gov/monitoring-content/teleconnections/nino-regions.gif⟩

Monthly anomalous (over Niño 3 region (5°N–5°S, 150°–90°W) and Niño 4 region (5°N–5°S, 160°E–150°W)) of SST indices are gathered from the NOAA Climate Prediction Center (⟨http://www.cpc.noaa.gov/data/indices/ersst4.nino.mth.81-10.ascii⟩). The locations of Niño 3 and Niño 4 regions are shown in figure 2.2. Niño 3 region is in red and Niño 4 region is in

blue. The black box indicates where Niño the 3.4 region (5°N-5°S, 170°-120°W) is located. These two indices are calculated using the ERSSTv4 data, ranging from 1950 to 2016, with the base period of 1981 to 2010.

2.4 Reanalysis data

The National Centers for Environmental Prediction and the National Center for Atmospheric Research (NCEP/NCAR) Reanalysis-1 monthly mean and 4-times daily data (Kalnay and Coauthors 1996) are collected from NSRL to perform the circulation analysis in the North Pacific region. This dataset has eight standard pressure levels from 1000 hPa to 300 hPa for specific humidity, 12 standard pressure levels from 1000 hPa to 100 hPa for vertical velocity, and 17 pressure levels from 1000 hPa to 10 hPa for zonal wind and meridional wind. The upward longwave radiation flux is calculated at the top of the atmosphere. The resolution of the upward longwave radiation flux is T62 Gaussian grid (192 $\times$ 94). For the rest of the variables, the resolution is global grids at 2.5° latitude $\times$ 2.5° longitude (144 $\times$ 73). The time range of this dataset is from 1948 to present. Variables that are used in this study are upward longwave radiation flux, specific humidity, u-wind, v-wind, sea level pressure, geopotential height and vertical velocity (ω).

CHAPTER 3
METHODOLOGY

3.1 Eastern Pacific and Central Pacific El Niño

Traditionally, ENSO is quantified by indices like SST anomalies in the Niño 3 region, Niño 4 region or Niño 3.4 region. However, studies (Larkin and Harrison 2005a,b; Kao and Yu 2009; Kug et al. 2009) show that some of the El Niño events has their largest SST anomalies in the eastern equatorial Pacific (EP) and some of the El Niño events has their largest SST anomalies in the central equatorial Pacific (CP). That is to say El Niño, the warmer phase of ENSO, has different flavors. There are also multiple methods to characterize these two types of ENSO (Eastern Pacific and Central Pacific; Ashok et al. (2007); Ren and Jin (2011); Takahashi et al. (2011)). In this study, the method of Ren and Jin (2011) is adopted to define these two types of El Niño. Let

$$\begin{aligned} N_{EP} &= N_3 - aN_4 \\ N_{CP} &= N_4 - aN_3. \end{aligned} \tag{3.1}$$

The subscripts EP and CP represent the Eastern Pacific El Niño and the Central Pacific El Niño, respectively. N_3 and N_4 denote Niño 3 and Niño 4 SST anomaly indices, respectively. When N_{EP} (N_{CP}) is positive and larger than one standard deviation of N_{EP} (N_{CP}) during winter (December through February), the warm SST anomalies can be defined as EP (CP) El Niño state. The transformation parameter a is chosen as $\frac{2}{5}$. This transformation parameter can reduce the correlation between Niño 3 and Niño 4 from a relatively high value of 0.73 to 0.13 but can still keep the high correlation between these two new indices and the N_3, N_4 indices. Figure 3.1 shows the detrend time series of N_{EP} (top) and N_{CP} (bottom). Red circles indicate the events that analyzed in this study. From the figure we can see that in the past 20 years, CP El Niño happens more frequently than EP El Niño. This result is consistent with Lee and McPhaden (2010). Table 3.1 summarizes the two types of El Niño events determined by this method. From the table we can see that there are ten EP events and eight CP events from 1956 to 2016.

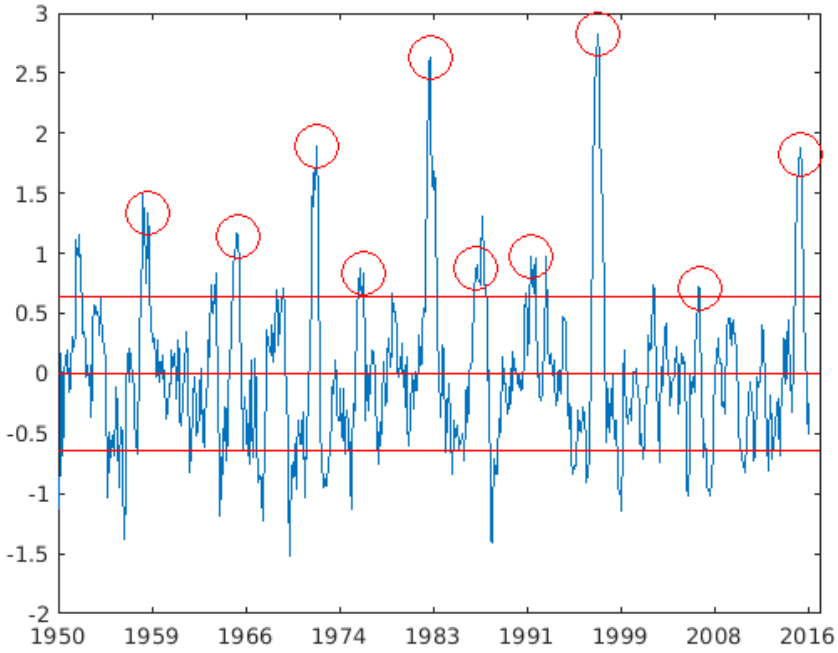

(a) EP

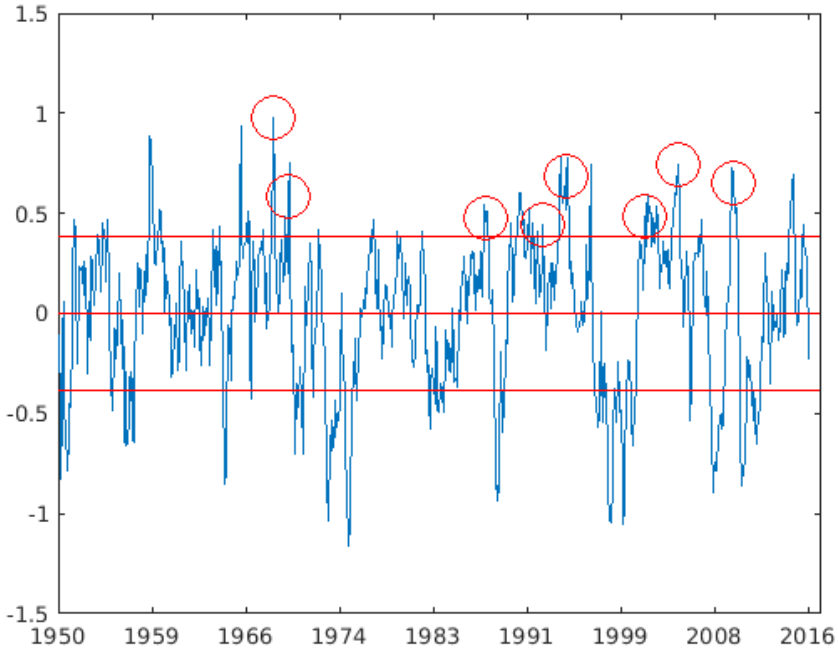

(b) CP

Figure 3.1: Time series of (a) N_{EP} and (b) N_{CP}. Red circles are the chosen events. Red lines indicate one standard deviation of N_{EP} and N_{CP}, respectively.

Table 3.1: CP and EP El Niño events

counts	years	events
1	1957-58	EP
2	1965-66	EP
3	1968-69	CP
4	1969-70	CP
5	1972-73	EP
6	1976-77	EP
7	1982-83	EP
8	1986-87	EP
9	1987-88	CP
10	1991-92	EP
11	1992-93	CP
12	1994-95	CP
13	1997-98	EP
14	2002-03	CP
15	2004-05	CP
16	2006-07	EP
17	2009-10	CP
18	2015-16	EP

3.2 Missing data filling

Many of the station rainfall data have months with missing values. To interpolate these missing values, we adopt two commonly used interpolation methods in this study. Then we compare the filling results to the origin data through a Q-Q plot to choose the best filling results. The two interpolation methods (http://home.uchicago.edu/~sctchoi/courses/cs138/interp.pdf) used in this study are described fully in Appendix A.

3.3 Moisture transport analysis

Horizontal moisture transport $\boldsymbol{f}$ can be represented in terms of specific humidity q and horizontal wind $\boldsymbol{V}$:

$$\mathbf{f} = q\mathbf{V}. \tag{3.2}$$

This function can be integrated throughout the atmosphere to vertically integrated water

vapor flux:

$$Q = \int_0^{\infty} \rho \mathbf{f} dz = \int_0^{P} \frac{\mathbf{f}}{g} dp, \tag{3.3}$$

where ρ indicates density, g indicates gravity and P indicates surface pressure. Since NCEP/NCAR reanalysis specific humidity is performed from 1000 hPa to 300 hPa, the vertical integration can be re-written using equations 3.2 and 3.3 as

$$Q = \frac{1}{g} \int_{300hPa}^{1000hPa} q\mathbf{V} dp. \tag{3.4}$$

Then we define moisture convergence and divergence as

$$\begin{aligned} C &= -\nabla \cdot Q \\ D &= \nabla \cdot Q, \end{aligned} \tag{3.5}$$

where C and D denote moisture convergence and divergence, respectively.

3.4 Nonparametric Wilcoxon-Mann-Whitney Rank Sum Test

The Wilcoxon-rank-sum test, also known as Wilcoxon-Mann-Whitney rank-sum test, was devised by Wilcoxon, and by Mann and Whitney independently in the 1940s (Wilks 2011). The null hypothesis is that the two populations are samples from the same distribution with equal medians. So the sample size of each sample data does not have to be the same. Suppose there are two batches of data with sample size n_1 and n_2. Under the null hypothesis, there is only one dataset with the sample size n=n_1 + n_2 drawing a single empirical distribution. Using the Mann-Whitney U-statistic,

$$U_1 = W_1 - \frac{n_1(n_1+1)}{2} \tag{3.6}$$

$$U_2 = W_2 - \frac{n_2(n_2+1)}{2} \tag{3.7}$$

where W_1 and W_2 are the sums of the ranks held by the two populations, respectively. Both U_1 and U_2 contain the same information. The null distribution of the Mann-Whitney U-statistic is an approximately Gaussian distribution when n_1 and n_2 are even moderately large values,

with

$$\mu_U = \frac{n_1 n_2}{2} \tag{3.8}$$

and

$$\sigma_U = \left[\frac{n_1 n_2 (n_1 + n_2 + 1)}{12}\right]^{\frac{1}{2}}. \tag{3.9}$$

Then compare the observed test statistic to the null distribution. If the test statistic falls in a sufficiently improbable region of the null distribution, the null hypothesis is rejected. However, not rejecting the null hypothesis does not mean that the null hypothesis is true. It means that there is insufficient evidence to reject the null hypothesis.

CHAPTER 4
DYNAMICAL DOWNSCALING

4.1 Regional Climate Model

The WRF-ARW model is a mesocale, compressible non-hydrostatic numerical weather model. This model has been widely used in dynamical downscaling in recent studies (Leung et al. 2006; Zhang et al. 2009, 2012). The WRF-ARW version 3.8 (Skamarock et al. 2008) was configured with one-way nesting for two domains (figure 4.1). The two nesting domains have horizontal resolutions of 10 km and 3.3 km. The second domain has 313 grid points in the east-west direction and 280 grid points in the north-south direction covering the entire Hawaiian Islands. There are 41 vertical levels from the surface to the 50 hPa level. The physic options in the simulation include WRF Single-Moment 6-Class Microphysics scheme (WSM6; Hong and Lim (2006)) for cloud microphysics processes, Community Atmospheric Model Version 3 radiation scheme (CAM3; Collins and Coauthors (2004)) for longwave and shortwave radiation fluxes, Yonsei University scheme (YSU; Hong et al. (2006)) for planetary boundary layer, Noah LSM (Chen and Dudhia 2001) for land surface processes and Tiedtke scheme (Wang et al. 2003, 2004) for the cumulus parameterization only for the outer domain. A summary of the physics schemes can be found in Table 4.1.

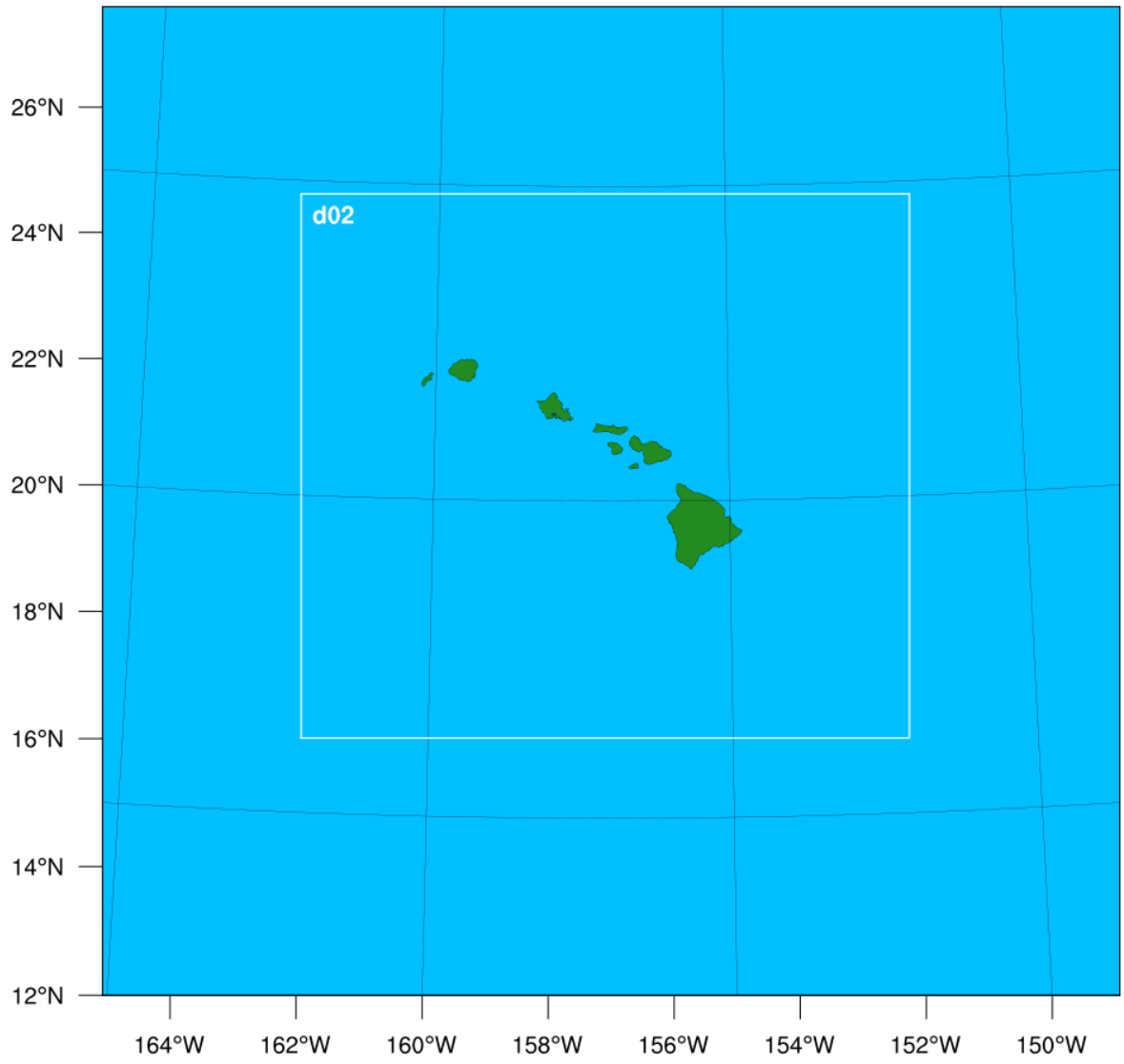

Figure 4.1: Model domains of the simulation.

4.2 Model Simulation

The model initial and lateral boundary conditions for the atmosphere were obtained from the European Center for Medium-Range Weather Forecasts (ECMWF) Re-Analysis Interim data (ERA-Interim) (Dee and Coauthors 2011). The ERA-Interim data downscaled in this study use reduced N128 (nominally 512 × 256) Gaussian grid and have 37 standard pressure levels from 1000 hPa to 1 hPa at 6-h intervals. The model was run twice for one EP winter

Table 4.1: The physics schemes chosen for the WRF model.

Physics	Scheme	Remarks
Cloud Microphysics	WRF Single-Moment 6-Class	A scheme with ice, snow and grapple processes suitable for high-resolution simulations.
Longwave Radiation and Shortwave Radiation	Community Atmospheric Model Version 3	Allows for aerosols and trace gases.
Boundary Layer Physics	Yonsei University	Non-local-K scheme with explicit entrainment layer and parabolic K profile in unstable mixed layer.
Land Surface Processes	Noah Land Surface Model	Soil temperature and moisture in four layers, fractional snow and frozen soil physics.
Cumulus Convection	Tiedtke	Mass-flux types schemes with CAPE-removal time scale, shallow component and momentum transport. Only for out domain.

(1991-92) and one CP winter (2002-03) since these two events have similar rainfall records to the averaged EP and CP winter rainfall records through station rainfall data analysis, respectively. The model was initialized at 0000 UTC December 1st and continuously until 0000 UTC March 1st for both EP and CP event. Nudging was turned on for both domains every six-hours.

CHAPTER 5
RESULTS

5.1 Rainfall Variability

Tables 5.1 and 5.2 show the summary of CP and EP winter (December though February) seasonal rainfall for the 21 stations, respectively. The climatology in the tables is defined as winter seasonal values from 1957 to 2016 (winter 1957 indicates December 1956 to February 1957). From Table 5.1 one can see that during EP winters, all stations show a drier than normal rainfall anomaly pattern (negative values). The Table 5.1 also shows how many missing months for each station. In Table 5.2, 19 of the 21 stations except for two stations in the leeward of Big Island, show that CP winters are slightly wetter than the winter climatological average. To ensure that this difference is not caused by only one extreme wet CP winter, this study calculates the truncated mean by discarding the largest and smallest values of rainfall during CP winters. Results still show that 16 of 21 stations are wetter than the winter climatology. A comparison between EP and CP winters can be found in Table 5.3. Under the column of CP minus EP, one can see that all the stations are wetter during CP winters relative to EP winters. For some stations, Honolulu airport as an example, the percentage of increased rainfall is larger than 100 %. For station Kihei which is located in the leeward side of Maui, CP winters have 241 % more rainfall than EP winters. Therefore, the El Niño-rainfall relationship as shown in Chu (1995) does not reveal the fact that Hawaii rainfall could very quite differently depending on the types of El Niño.

5.2 Circulation variability

Commonly, Hawaii experiences drier winter conditions during El Niño years (Chu 1995; Chu and Chen 2005). The results from this study show that during CP winters the Hawaiian Islands are wetter than EP winters. For some stations, also during CP winters, the Hawaiian Islands are even slightly wetter than the winter rainfall climatology. While during EP winters, the Hawaiian Islands are very dry compared to winter climatology. In this section, we compare the large scale circulation difference between CP and EP winters to find some physical mechanisms that may cause this rainfall difference. First, we will analyze the SST difference, as shown in figure 5.1, since we define EP and CP El Niño based on SST anomalies.

Table 5.1: EP winter precipitation summary for all 21 stations in Hawaii. The units of precipitation values are in millimeters. Winter is defined as December through February from 1957 to 2016 (for example, winter 1957 means December 1956, January and February 1957). Different islands are separated by single lines for Kauai, Oahu, Maui and Hawaii, in that order.

	Station	Missing month(s) (724 months in total)	1956-2016 winter total (mm)	EP winter total (mm)	EP anomalies (mm)
1	Lihue airport	0	333.84	179.97	-153.87
2	Manoa	21	474.00	312.54	-161.46
3	Manoalua	25	306.33	166.14	-140.19
4	Palolo	59	819.78	678.78	-141.00
5	Punchbowl	1	301.77	184.98	-116.79
6	Pauoa	34	917.73	719.76	-197.973
7	Honolulu airport	0	203.34	102.30	-101.04
8	Waialae (spline)	13	271.44	173.01	-98.43
9	Nuuanu	31	678.84	458.49	-220.35
10	Kalihi	30	719.25	522.00	-197.25
11	UH	17	319.68	209.64	-110.04
12	Puunene	10	229.32	161.61	-67.71
13	Kahului Airport	3	218.43	119.43	-99.00
14	Sperckelsville	10	249.78	155.55	-94.23
15	Kihei	14	174.84	68.67	-106.17
16	Hamakuapoko	7	375.60	269.73	-105.87
17	Hilo airport	0	790.89	515.16	-275.73
18	Paauilo	1	720.45	538.62	-181.83
19	Papaikou (pchip)	77	869.46	492.84	-376.62
20	Kainaliu	42	228.81	111.27	-117.54
21	Naalehu	17	375.48	178.29	-197.19

Table 5.2: CP winter precipitation summary for all 21 stations in Hawaii. The units of precipitation values are in millimeters. Winter is defined as December through February from 1957 to 2016 (for example, winter 1956 means December 1956, January and February 1957). Different islands are separated by single lines for Kauai, Oahu, Maui and Hawaii, in that order.

	Station	1956-2016 winter total (mm)	CP winter total (mm)	CP anomalies (mm)	CP truncated mean anomalies (mm)
1	Lihue airport	333.84	339.27	+5.43	-22.92
2	Manoa	474.00	529.20	+55.20	+45.24
3	Manoalua	306.33	322.59	+16.26	-0.75
4	Palolo	819.78	930.06	+110.28	+115.95
5	Punchbowl	301.77	330.36	+28.59	+8.13
6	Pauoa	917.73	1028.67	+110.94	+90.39
7	Honolulu airport	203.34	231.00	+27.66	+4.38
8	Waialae (spline)	271.44	284.34	+12.90	-1.74
9	Nuuanu	678.84	800.73	+121.89	+57.24
10	Kalihi	719.25	915.60	+196.35	+154.44
11	UH	319.68	368.13	+48.45	+20.73
12	Puunene	229.32	254.64	+25.32	+11.25
13	Kahului Airport	218.43	248.04	+29.61	+19.53
14	Sperckelsville	249.78	270.81	+21.03	+6.51
15	Kihei	174.84	234.00	+59.16	+43.8
16	Hamakuapoko	375.60	400.5	+24.9	+11.13
17	Hilo airport	790.89	1029.00	+238.11	+151.11
18	Paauilo	720.45	964.89	+244.44	+151.29
19	Papaikou (pchip)	869.46	1071.39	+201.93	+120.36
20	Kainaliu	228.81	200.85	-27.96	-50.58
21	Naalehu	375.48	358.50	-16.98	-58.44

Table 5.3: Station data comparison between CP and EP El Niño winters. The units of precipitation values are in millimeters. Different islands are separated by single lines for Kauai, Oahu, Maui and Hawaii, in that order.

	Station	CP-EP (mm)	CP/EP	(CP-EP)/EP
1	Lihue	+159.30	1.89	89%
2	Manoa	+216.69	1.69	69%
3	Manoalua	+156.48	1.94	94%
4	Palolo	+251.31	1.37	37%
5	Punchbowl	+145.38	1.79	79%
6	Pauoa	+308.91	1.43	43%
7	Honolulu airport	+128.37	2.26	126%
8	Waialae (spline)	+111.33	1.64	64%
9	Nuuanu	+342.27	1.75	75%
10	Kalihi	+393.60	1.75	75%
11	UH	+158.49	1.76	76%
12	Puunene	+93.00	1.58	58%
13	Kahului Airport	+128.64	2.08	108%
14	Sperckelsville	+115.26	1.74	74%
15	Kihei	+165.30	3.41	241%
16	Hamakuapoko	+130.77	1.48	48%
17	Hilo airport	+513.84	1.00	100%
18	Paauilo	+426.27	1.79	79%
19	Papaikou (pchip)	+578.58	2.17	117%
20	Kainaliu	+89.55	1.80	80%
21	Naalehu	+180.18	2.01	101%

From Fig. 5.1a, one can clearly see that, climatologically, there are warmer SST in the tropical western Pacific ocean and lower SST in the southeast Pacific ocean. The relatively warm water is also found to the south of the Hawaiian Islands. During EP winters (Fig. 5.1b), the warm SST anomalies occur in the cold tongue region in the equatorial eastern Pacific with a western extension to the central Pacific while the warm pool region in the equatorial western Pacific becomes cooler. During CP winters (Fig. 5.1c), although the cold tongue region is still warmer than climatology, the warmest SST shifts to the equatorial central Pacific ocean. In this case, the Hawaiian Islands are surrounded by relatively warm water. Comparing CP winters to EP winters, as shows in the Fig. 5.1d, the largest warm SST anomalies occur in the equatorial central Pacific and the SST southwest of the Hawaiian Islands are relatively warmer. The crosses in Fig. 5.1b, c and d indicate the grids that pass the 90% significant level of nonparametric Wilcoxon-Mann-Whitney rank-sum test. Passing the test means that the null hypothesis that the two data samples (EP and CP) are from the same distribution is rejected at the 10 % rejection level.

Large scale circulation at the 1000 hPa level is analyzed in figure 5.2. Fig. 5.2a is the wind field and sea level pressure climatology. From Fig. 5.2a one can see that the Aleutian low is located to the northwest of Hawaii and the subtropical high is to the northeast of Hawaii, which brings northeast trade winds to the islands. The wind anomalies between EP and climatology, CP and climatology, CP and EP are shown in figures 5.2b to 5.2d. Fig. 5.2b shows that during EP winters, Hawaii has northerly to northeasterly wind anomalies north to the Islands. The Aleutian low is deeper during EP winters. During CP winters (Fig. 5.2c), the north and northeast wind anomalies shifted slightly to the west so the wind anomalies in the vicinity of Hawaii show a northwest anomalous pattern. Comparing CP to EP (Fig. 5.2d), an anomalous cyclonic circulation and southwesterly anomalies prevail in the vicinity of Hawaii. That is to say, compared to EP winters, CP winters have southwesterly wind anomalies.

At the 850 hPa level, wind and geopotential height climatology are shown in figure 5.3a. Wind anomalies and geopotential height anomalies between EP and climatology, CP and climatology and CP and EP are presented in figures 5.3b to d, respectively. During EP winters (Fig. 5.3b), the anomalously cyclonic circulation immediately to the northeast of the Hawaiian Islands brings northerly wind to the north of the Islands. But to the west of the Islands, the anomalous wind direction is northwest which diminishes the northeast trade wind. During CP winters (Fig. 5.3c), the anomalously cyclonic circulation is shifted northeastward toward the west coast of North America and westerly and southwesterly wind

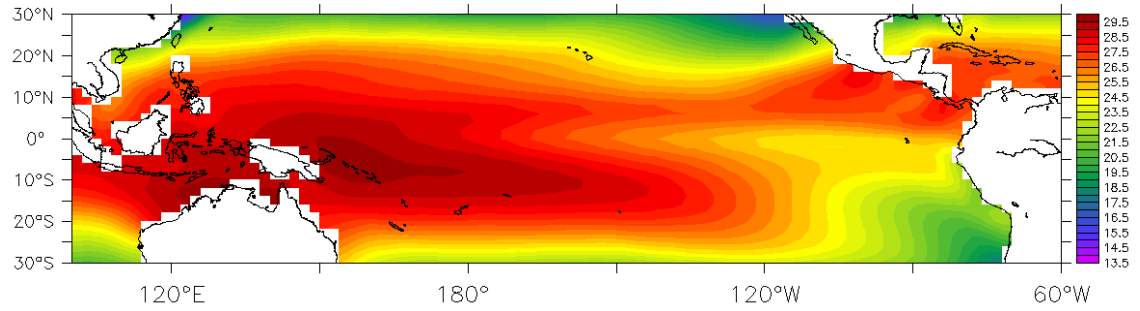

(a) Winter climatology

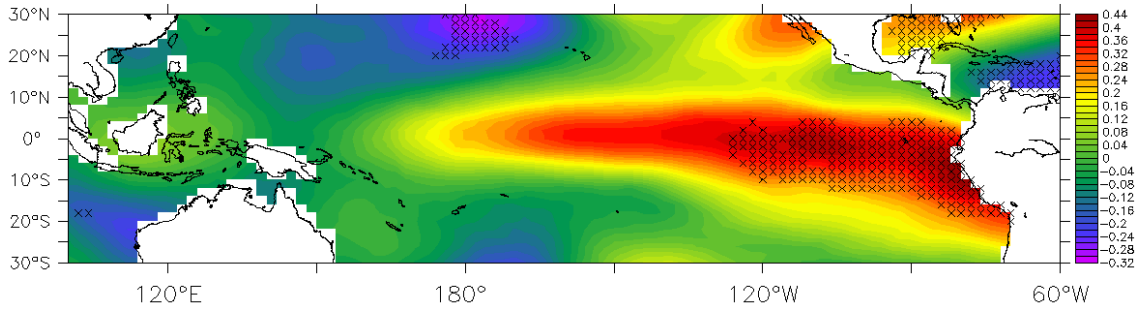

(b) EP anomalies

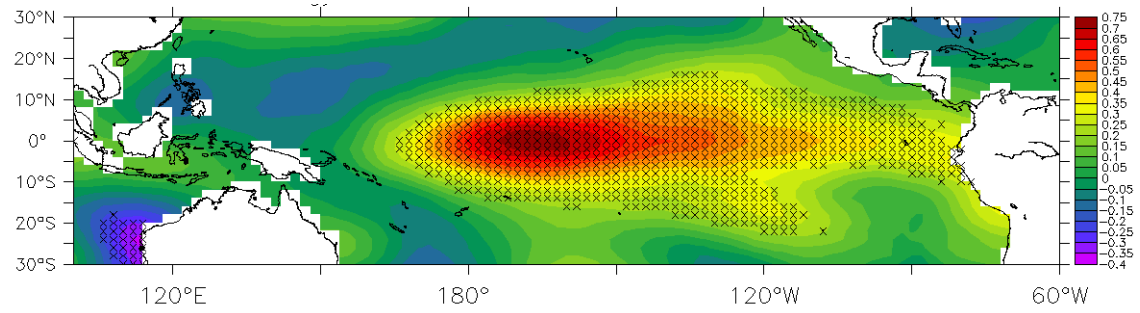

(c) CP anomalies

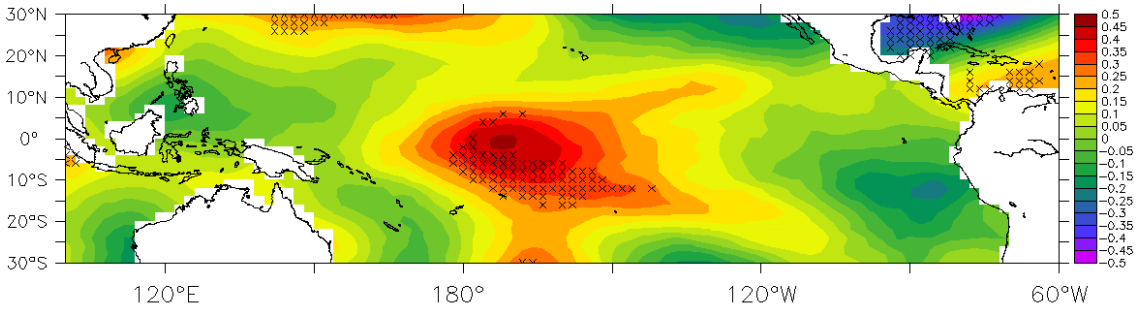

(d) CP minus EP

Figure 5.1: Winter SST of (a) climatology, (b) EP minus climatology, (c) CP minus climatology and (d) CP minus EP. The unit is °C. Crosses in panel (b) (c) and (d) indicate the grid boxes that pass 90% significance test.

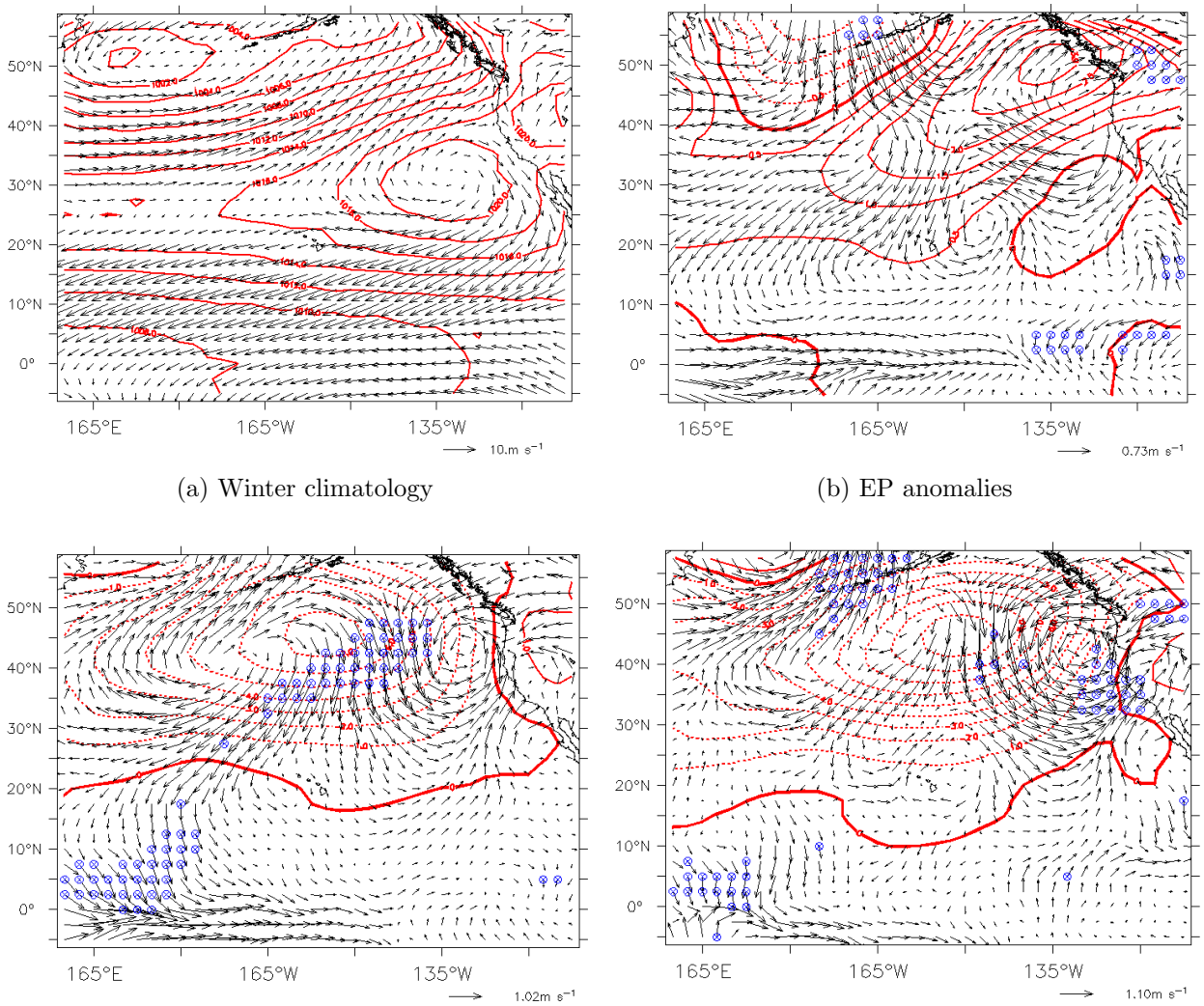

(a) Winter climatology

(b) EP anomalies

(c) CP anomalies

(d) CP minus EP

Figure 5.2: Winter large scale circulation at the 1000 hPa surface level. Panel (a) shows the climatology, contours are sea level pressure from 1002to 1020 hPa with a 2 hPa interval and wind vectors. Panels (b), (c) and (d) are for EP anomalies, CP anomalies and CP minus EP, respectively. Vectors are wind anomalies; contours indicate sea level pressure anomalies and dashed lines are negative anomalies. Crosses indicate the grid boxes that pass 90% significance test for v-wind.

anomalies prevail over the Hawaiian Islands. The difference between CP and EP winters is also marked by anomalous southwesterly winds (Fig. 5.3d). The southwesterly anomalies appear at the leeward side of the Islands and across the island chain.

Results analyzed at the 1000 hPa and 850 hPa levels are consistent with Timm and Diaz (2009), who find that southerly wind anomalies in the lower atmosphere (1000 hPa) can increase the precipitation throughout the Islands.

At the 200 hPa level, the wind field is shown in figure 5.4 for (a) climatology, (b) EP anomalies, (c) CP anomalies and (d) CP minus EP. Wind speeds stronger than 25 ms^{-1} are shaded in Fig. 5.4a. The climatological jet stream contour is in panel (b) and panel (c). The EP jet stream contour is in panel (d) for comparison with CP jet stream position. Green (blue) shadings are positive (negative) wind speed anomalies. From Fig. 5.4a one can see, during northern hemisphere winter, the subtropical jet stream core (defined as wind speeds larger than 40 ms^{-1}) is near 35°N extending from the western Pacific to the central Pacific and to the north of Hawaii. During EP winters (Fig. 5.4b), the position of the jet stream is shifted to the south, as one can see that the green shadings are south to the climatological position of the jet stream and one can also see the positive wind speed anomalies over the Hawaiian Islands. Very warm SSTs in the eastern Pacific associated with EP El Niño can enhance the temperature gradient from the equator to the polar regions, as a result of angular momentum transport by the Hadley circulation (Held and Hou 1980), the subtropical jet stream is shifted to the south. Hawaii is located in the right exit region of the jet which favors sinking motion and divergence in the lower troposphere (Chu 1995). During CP winters (Fig. 5.4c), the larger changes of the subtropical jet stream are shifted to the eastern Pacific and east of Hawaii which tend to steer storms to the west coast of the United States. The wind direction anomalies can be presented more clearly from the CP minus EP panel (Fig. 5.4d). Relative to EP, CP has southerly wind anomalies over Hawaii. An anomalously cyclonic cell is noted to the west of the Hawaiian Islands and an anti-cyclonic wind anomaly east of the Hawaiian Islands. Over the Hawaiian Islands, there are cyclonic and southerly wind anomalies.

Figure 5.5 shows the (a) climatology, (b) EP anomalies, (c) CP anomalies, and (d) CP minus EP north-south vertical circulation. The north-south vertical cross section is obtained by averaging the meridional wind between 165°W to 150°W and then combining it with negative pressure vertical velocity (-ω) at eight standard pressure levels from 1000 hPa to 300 hPa. Specific humidity is in shading. The range of the Hawaiian Islands are represented by the two vertical lines. Figure 5.5a indicates that there are descending motions from the upper

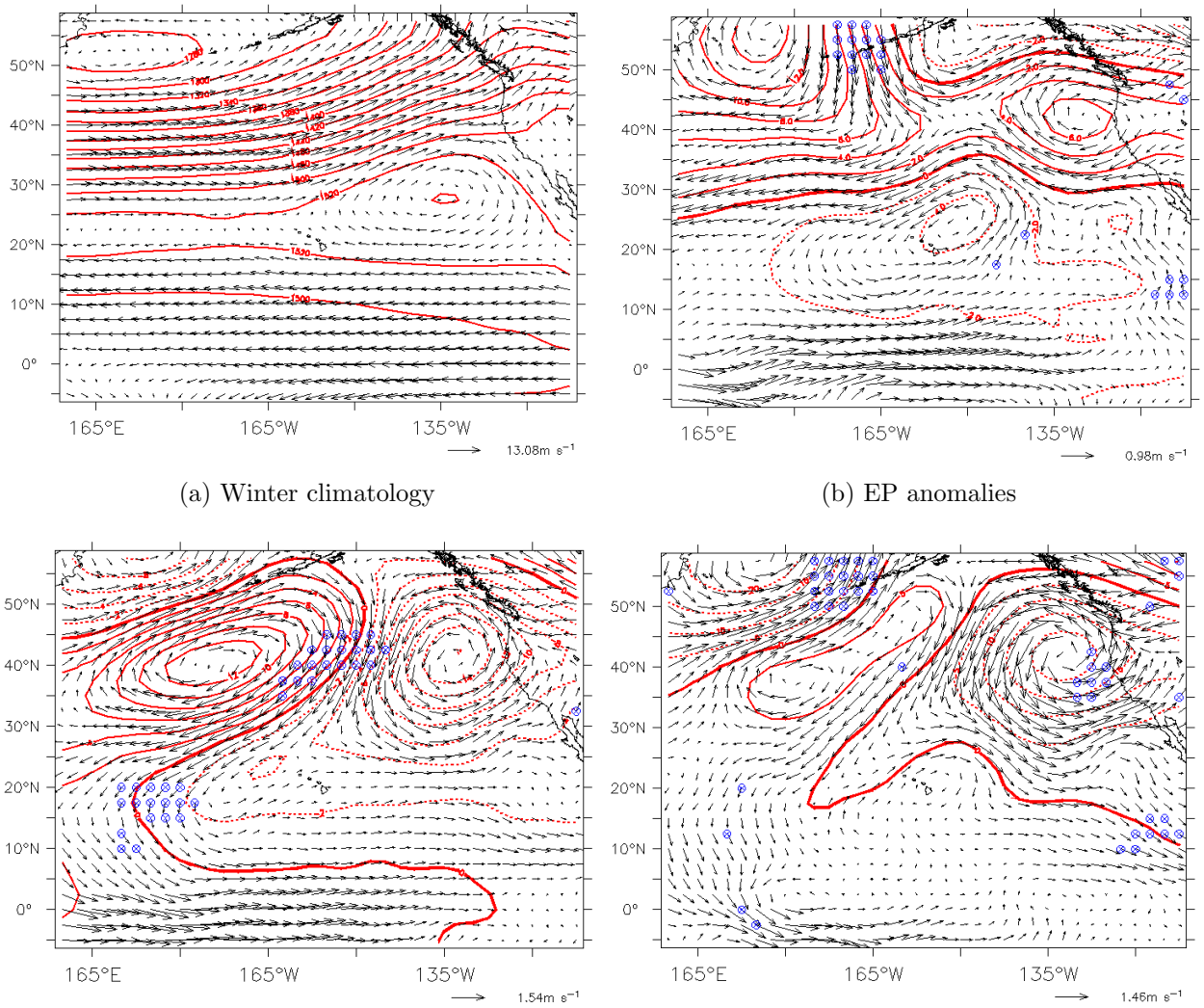

(a) Winter climatology

(b) EP anomalies

(c) CP anomalies

(d) CP minus EP

Figure 5.3: Winter large scale circulation at the 850 hPa level. Panel (a) shows the climatology, contours are geopotential height from 1280 to 1520 geopotential meters with a 20 geopotential meters interval and wind vectors. Panels (b), (c) and (d) are for EP anomalies, CP anomalies and CP minus EP, respectively. Vectors are wind anomalies; contours indicate geopotential height anomalies and dashed lines are negative anomalies. Crosses indicate the grid boxes that pass 90% significance test for v-wind.

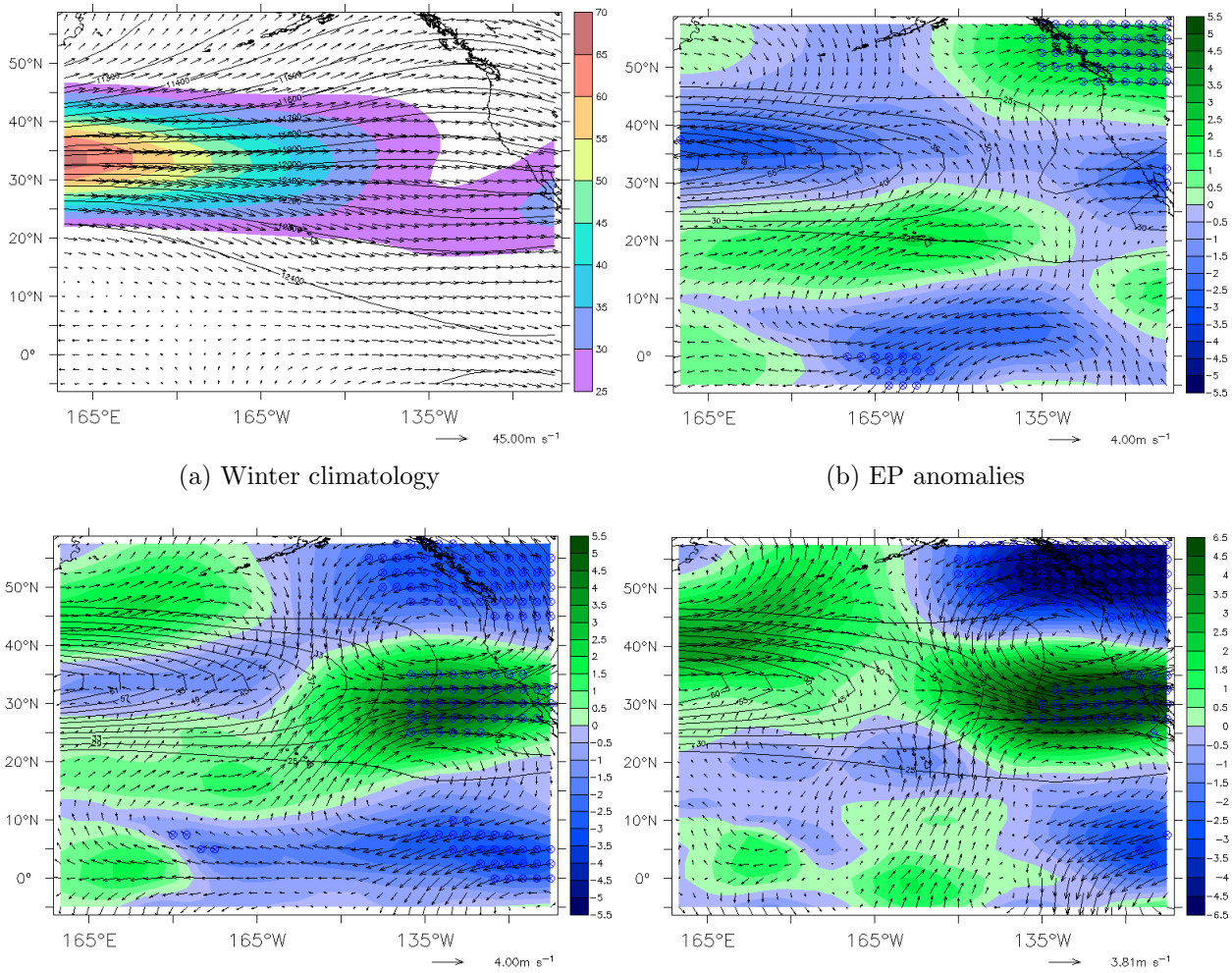

(a) Winter climatology

(b) EP anomalies

(c) CP anomalies

(d) CP minus EP

Figure 5.4: Winter large scale circulation at 200 hPa level. Panel (a) shows the climatology, contours are geopotential height from 11300 to 12400 geopotential meters with a 100 geopotential meters interval, wind vectors and shading for wind speeds that are larger than 25 m/s. Panels (b) and (c) are for EP anomalies, CP anomalies respectively; contours indicate climatology subtropical jet stream position, vectors are wind anomalies and shadings are wind speeds anomalies with positive anomalies in green. Panel (d) indicates CP winters minus EP winters, contours are EP winter subtropical jet stream position, vectors are wind anomalies and shadings are wind speeds anomalies with positive anomalies in green. Crosses indicate the grid boxes that pass 90% significance test for wind speeds.

troposphere to the lower troposphere over the Hawaiian Islands. South of the Islands, there are Hadley type ascending motion near the equator. Specific humidity is concentrated in the lower troposphere and near 15°S. During EP winters (Fig. 5.5b), anomalous descending motion is found in the lower troposphere and anomalous ascending motion is found in the upper troposphere with negative specific humidity anomalies over the Hawaiian Islands. During CP winters (Fig. 5.5c), anomalous ascending motion is found at all vertical levels and positive specific humidity anomalies are found over the Hawaiian Islands. Comparing CP to EP (Fig. 5.5d), there are anomalous ascending motions and positive specific humidity anomalies over the Hawaiian Islands. Compared to EP winters, CP winters have weaker descending motion and more specific humidity over the Islands.

An additional insight into the difference of Hawaii winter rainfall between CP and EP episodes can be gained by examining the vertically integrated moisture flux and moisture flux divergence. Figure 5.6 indicates (a) climatology, (b) EP anomalies, (c) CP anomalies and (d) CP minus EP, respectively. From Fig 5.6a one can see that the Hawaiian Islands are located in the subtropical moisture flux divergence area. There is moisture flux convergence near the equator and at the midlatitudes. Because Hawaii is located in the descending branch of the Hadlay cell, moisture flux divergence is expected. The moisture flux convergence near the equator is due to the trade wind convergence in the Inter Tropical Convergence Zone (ITCZ). Comparing EP to climatology (Fig. 5.6b), except for Big Island, other Islands are under anomalous moisture flux divergence area with the moisture flux being transported southwestward by drier air. Figure 5.6c shows the CP winter anomalies. During CP winters, the Hawaiian Islands are under anomalous moisture flux convergence with westerly moisture transport. If we compare the difference between CP and EP winters (Fig. 5.6d), we find that even though Hawaii is surrounded by moisture flux divergence areas, moisture flux convergence areas are noted in a small patch extending from southwest to northeast across the Islands. This pattern supports that CP winters are wetter than EP winters.

The outgoing longwave radiation (OLR) flux at the top of the atmosphere is also analyzed in this study. Regarding OLR measured from the NOAA polar-orbiting satellite, the infrared sensor detecting longwave radiation emitted from the Earth is in the 10.5 - 12.5 μm wavelength band. In the case of deep convective clouds, the sensor measures radiation from the top of clouds. For clear sky, the satellite radiation monitors longwave radiation emitted mainly from the Earth's surface. In the tropics, the OLR mainly represents cloud-top temperatures, with low values corresponding to cold and high clouds, which generally denote enhanced convection. The unit of the OLR flux is Wm^{-2}. Figure 5.7 indicates the OLR flux for (a)

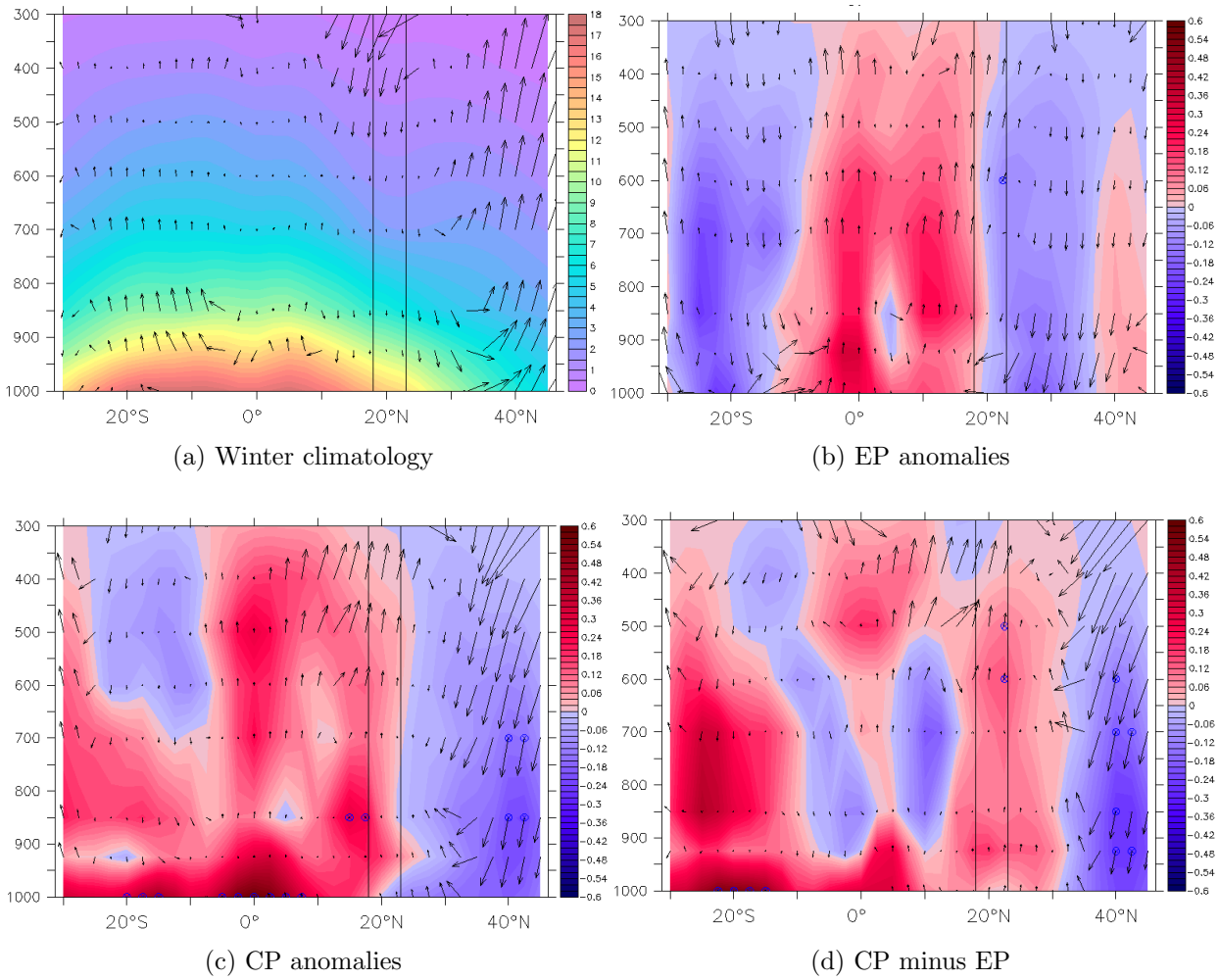

(a) Winter climatology

(b) EP anomalies

(c) CP anomalies

(d) CP minus EP

Figure 5.5: Meridional winter wind and vertical winter wind cross section (vector) with specific humidity (shading). All the variables are averaged between 165°W to 150°W. Hawaiian Islands are located approximately between the two vertical lines. Vectors and shadings in panels (b), (c) and (d) are wind anomalies and specific humidity anomalies with positive anomalies in red. Crosses indicate the grid boxes that pass the 90% significance test for specific humidity.

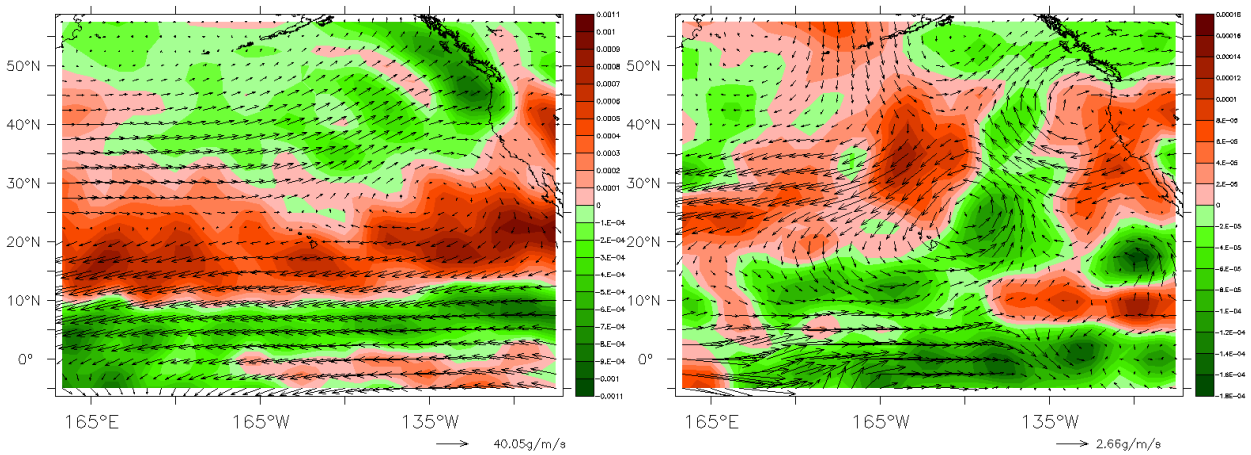

(a) Winter climatology

(b) EP anomalies

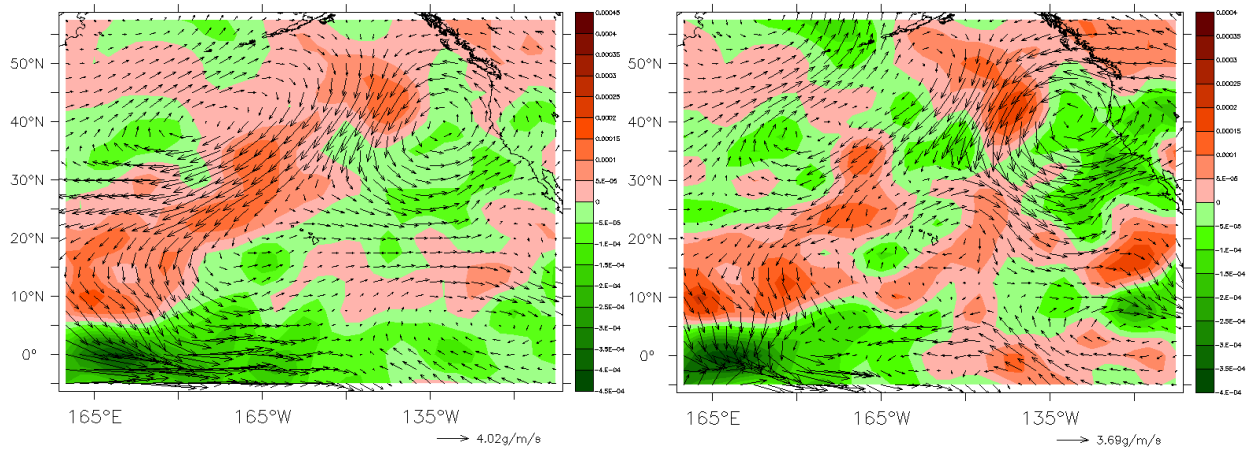

(c) CP anomalies

(d) CP minus EP

Figure 5.6: Moisture flux transport (vector) and moisture flux divergence and convergence (shading). Panel (a) is winter climatology from 1957 to 2016, red (green) shading indicates moisture flux divergence (convergence). Vectors in panels (b), (c) and (d) are moisture flux anomalies and red (green) shadings are moisture flux divergence (convergence) anomalies.

climatology, (b) EP anomalies, (c) CP anomalies and (d) CP minus EP. From Fig. 5.7a one can see that lower OLR values are located in the equatorial western Pacific which indicate that there might be more convective systems over this area. Figure 5.7b shows that during EP winters, positive anomalies occur in the cold south-east Pacific and negative anomalies occur in the central equatorial Pacific region. The Hawaiian Islands have a slightly positive OLR flux anomaly except for Big Island, implying relatively cloudless skies during EP winters. While during CP winters (Fig. 5.7c), the positive anomalies occur in the west Pacific region and northeast Pacific region. Along the equator, there are negative OLR flux anomalies. Over the Hawaiian Islands, there are slightly negative OLR flux anomalies. Comparing CP to EP winters (Fig. 5.7d), the Hawaiian Islands are located in the negative outgoing longwave radiation flux region. That is to say, there might be more clouds over the Hawaiian Islands during CP winters compared to EP winters. This result is consistent with the moisture flux analysis (Fig. 5.6).

5.3 Case study

To show a more detailed wind field and precipitation pattern over the Hawaiian Islands, a dynamical downscaling simulation was run using the WRF-ARW model. In this study, 10 EP and eight CP events were averaged to analyze the station rainfall and large circulation difference. It is very expensive to run the WRF-ARW model for 18 times individually. Instead, one EP and one CP event were chosen. To pick which events to use in the simulation, station rainfall data of each event was compared to the averaged EP and CP events of all rainfall records for the 21 stations. EP and CP events closest to the averaged events were then selected. Here, the 1991-92 December through February (DJF) was chosen for the EP event and 2002-03 DJF was chosen for the CP event. Then a composite for a three-month run was calculated to make the comparison between EP and CP events.

5.3.1 Wind Field Simulation

For the 1000 hPa level wind field simulation (Fig. 5.8), one can see, for the EP event (Fig. 5.8a), east to northeast trade winds prevail over the Islands and strong trades flow cross the Island channels. Big Island has a clear island effect on the trade winds. For the CP event (Fig. 5.8b), northeast trade winds are still evident over the Islands. However, the wind direction east of the Big Island is almost easterly and the wind direction east of Maui has a southerly component due to the island effect. The wind anomalies between CP and

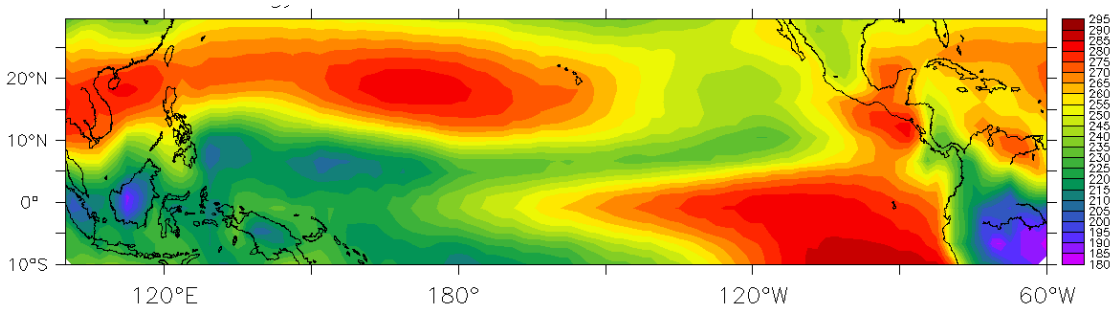

(a) Winter climatology

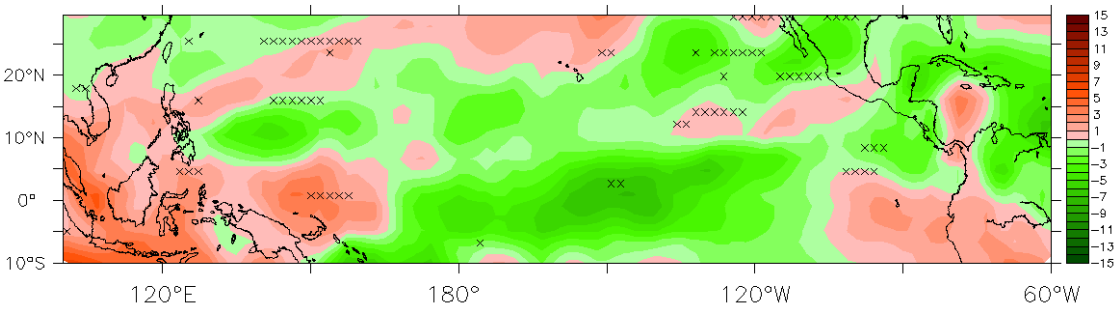

(b) EP anomalies

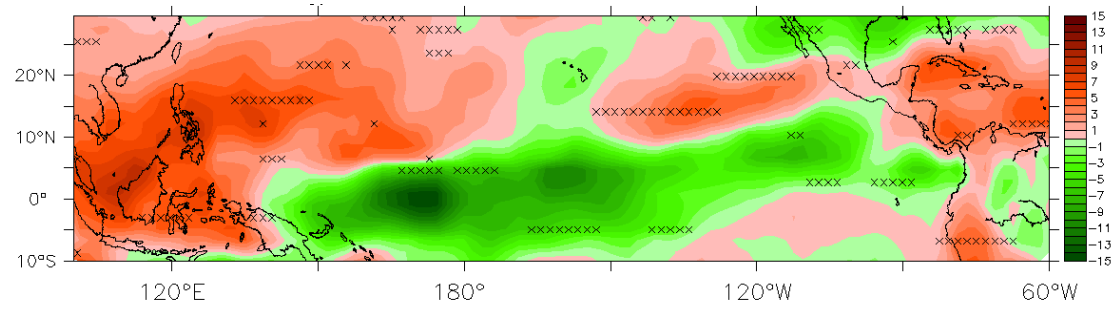

(c) CP anomalies

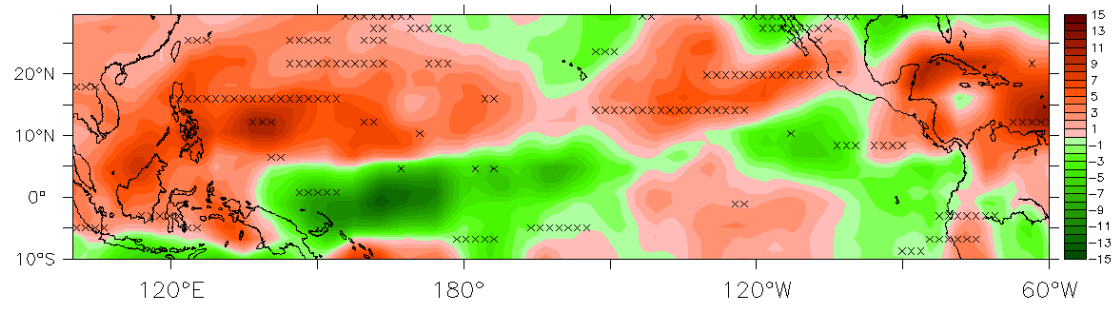

(d) CP minus EP

Figure 5.7: Winter outgoing longwave radiation flux (unit: W/m^2) on top of the atmosphere (a) climatology, (b) outgoing longwave radiation flux anomalies on top of the atmosphere of EP minus climatology, (c) CP minus climatology and (d) CP minus EP. Crosses indicate the grid boxes that pass the 90% significance test.

EP event are shown in Fig. 5.8c. Consistent with large circulation analysis, one can find southwest wind anomalies southwest of the Islands. East of the Islands, there are southerly wind anomalies. The dynamical downscaling simulation yields detailed wind fields in which CP winter has a weaker northerly wind component in the study domain.

Figures 5.9a to 5.9c show the 850 hPa level wind field simulation of the EP event, CP event and CP minus EP anomalies. At this level, although east to northeast trades prevail over the Islands, the island blocking effects are more clear comparing to 1000 hPa level (Fig. 5.8). From the EP event (Fig 5.9a), to the east of Maui, southeast winds are found. To the west of Maui and Big Island, the winds are relatively weak. For the CP panel (Fig. 5.9b), the south component of the southeast winds are stronger. Not only east of Maui and Big Island, but also east of Oahu, there are southeast winds. Northeast trades are not found in this panel even south to 18 °N where one can find northeast trades in the EP panel (Fig. 5.9a). The wind field difference between CP and EP events can be found in Fig. 5.9c. Southwest wind anomalies appear in the western part of the Island chain except for the Kona area of Big Island where there appears to be return flow. In the Kona area of Big Island, return flow is stronger during the CP event.

5.3.2 Rainfall Simulation

The WRF-ARW rainfall simulations are shown in Fig. 5.10. As shows in EP panel (Fig. 5.10a), the windward slopes receive the most rainfall and the leeward slopes are drier state wide. For CP (Fig. 5.10b) event, the rainfall distribution is still the same. However, for the wettest areas (red shadings in Fig. 5.10a), CP has less rainfall simulated. Focusing on the CP minus EP event, there is more rainfall on the leeward side of Maui and Big Island. These positive anomalies may be caused by stronger return flow during CP event as compared to EP event. However, the simulation is inconsistent with station data that all stations are wetter during CP events compared to EP events which is discussed previously in section 5.1. For the reason why the rainfall simulation is inconsistent with the 21 station analysis, more research needs to be done. In this study, the Hawaiian rainfall atlas maps will be used to perform further analysis on the rainfall variance during EP and CP winters, which will be discussed in the next section.

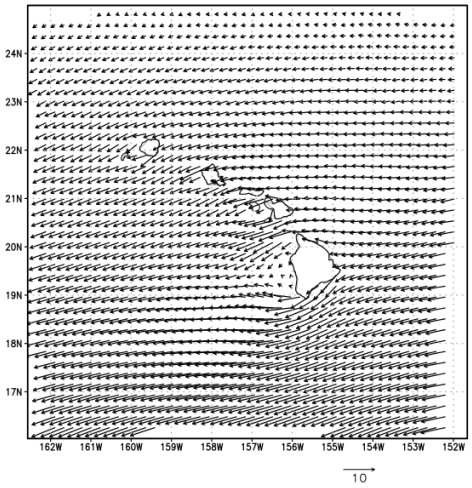

(a) EP

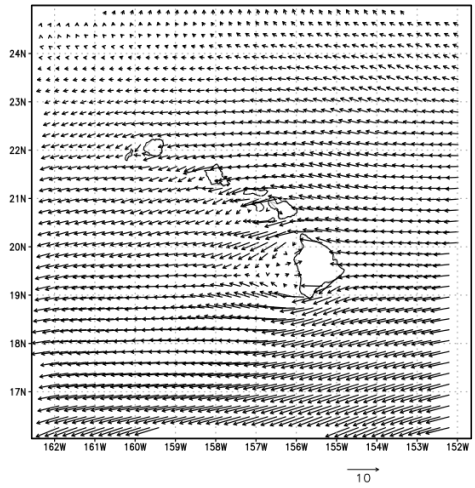

(b) CP

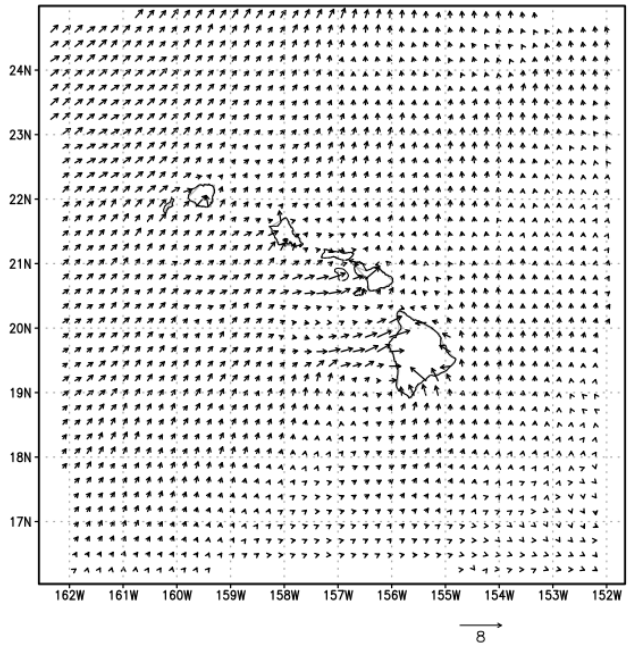

(c) CP-EP

Figure 5.8: 1000 hPa level wind field simulation for (a) EP event, (b) CP event and (c) CP minus EP. The unit of wind speed is in m/s.

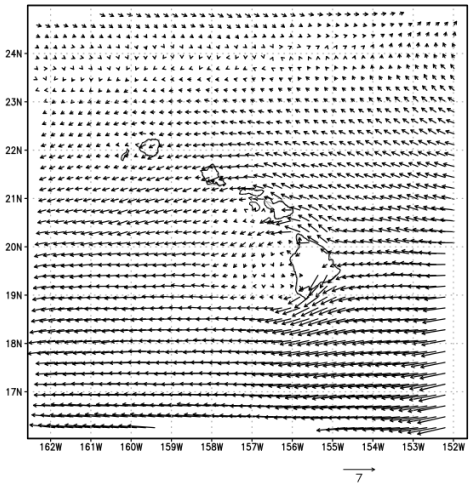

(a) EP

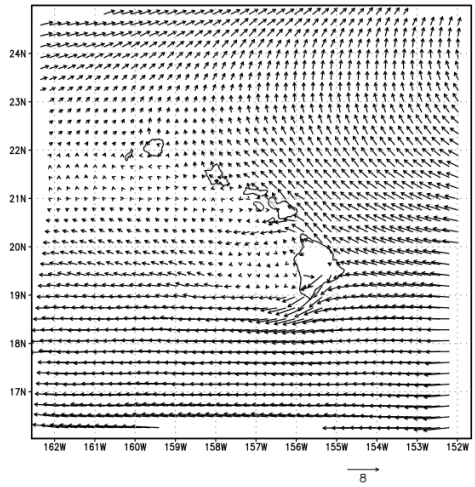

(b) CP

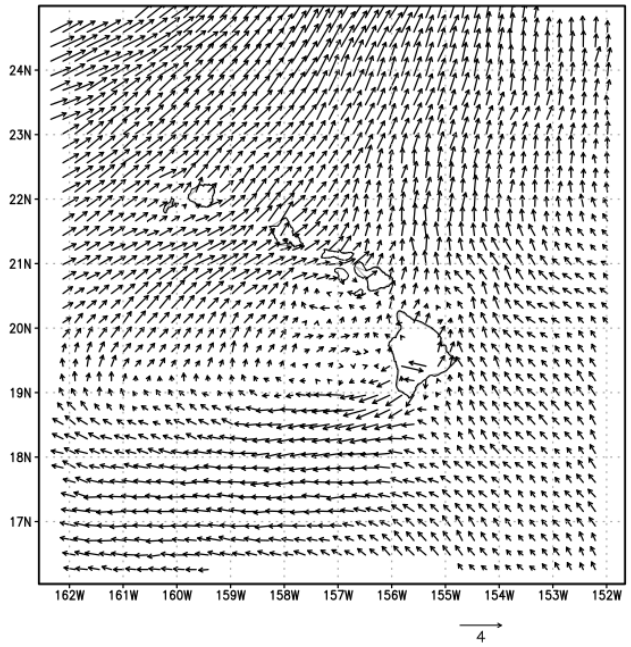

(c) CP-EP

Figure 5.9: 850 hPa level wind field simulation for (a) EP event, (b) CP event and (c) CP minus EP. The unit of wind speed is in m/s.

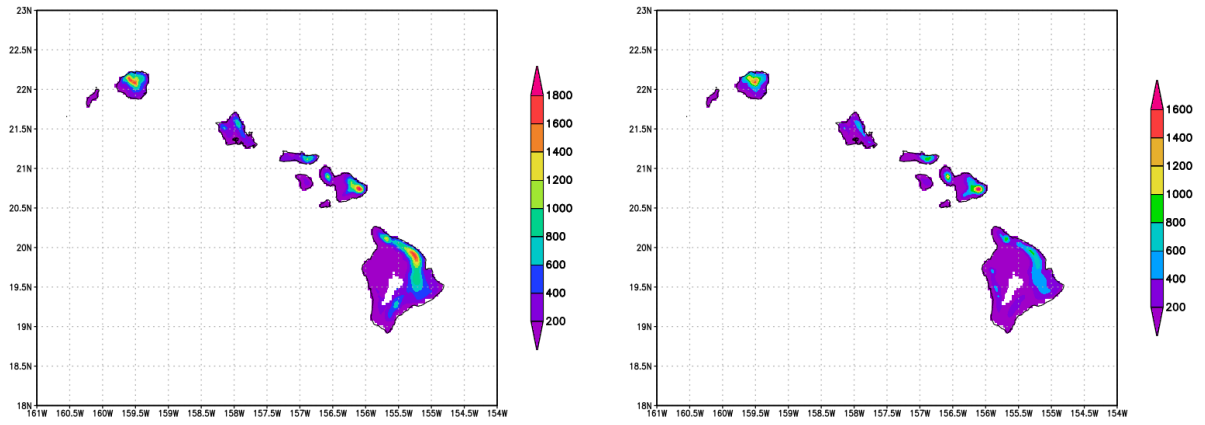

(a) EP

(b) CP

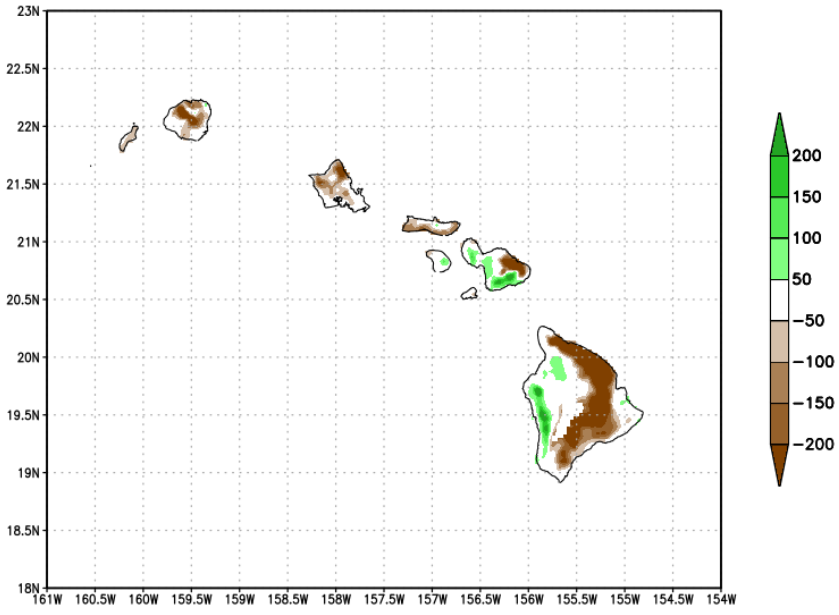

(c) CP-EP

Figure 5.10: WRF-ARW simulation of rainfall. (a) is for EP event, (b) is for CP event and (c) is CP winter rainfall simulation minus EP winter rainfall. For (a) and (b), red shadings indicate more rainfall areas and purple shadings indicate less rainfall areas. For (c), green shadings are for positive rainfall anomalies and brown shadings are for negative anomalies. The color bars for (a) are from 200 mm to 1800 mm, for (b) are from 200 mm to 1600 mm and for (c) are -200 mm to 200 mm.

5.4 Hawaiian Rainfall Atlas

The Rainfall Atlas of Hawaii (Giambelluca et al. 2013) is a set of maps of spatial distributions of major Hawaiian Islands rainfall. Over 1,000 stations were used to develop the approximately 234 $\times$ 250 m resolution rainfall maps. In this section, the maps of EP winter rainfall anomalies, CP winter rainfall anomalies and CP winter minus EP rainfall anomalies are discussed. These maps are originally from Abby G. Frazier through personal communication.

From figure 5.11a, one can see during EP winters, Hawaii is drier than normal station wide. The dark brown areas in the figure are the areas which receive less rainfall. Usually these areas receive a lot of precipitation on average. This drier than average EP winter rainfall result is consistent with the station analysis that all 21 stations are drier than winter climatology. For Fig. 5.11b, instead of state wide drier-than-normal patterns like EP winters, CP winter rainfall anomalies vary from area to area. For Kauai, the lower-lands are wetter than climatology while higher elevations are drier than climatology. For Oahu, most of the areas are wetter during CP winter except for north shore, lee side and the east part of central Oahu. The rainfall anomalies calculated from Rainfall Atlas of Hawaii of both Kauai and Oahu are consistent with the station data analysis. The west and central Maui show a dipole rainfall anomalous pattern in that the south side is drier and the north side is wetter. The upcountry area of Maui is drier during CP winters and east Maui is wetter except for the Haleakala area. For Big Island, the Kona area, east part of Puna area and north part of Hamakua area are wetter during CP winters. The rest of the Islands are drier than the winter climatology during CP winters. When using CP winter rainfall minus EP winter rainfall (5.11c), all the Islands are wetter during CP winters, which again, is consistent with the 21 station data analysis.

5.5 Synoptic System Difference

Results from the winter synoptic systems relevant to CP and EP episodes are discussed in this section. The resources that used to count the synoptic systems include NCEP/NCAR Reanalysis-1 4-times daily data, National Weather Service (NWS) tropical strip 250 MB analysis charts, NWS tropical strip surface analysis and observations charts and State of Hawaii monthly precipitation summary from Kevin Kodama through personal communication. Table 5.4 shows the counts of upper level troughs, upper level lows, Kona lows and cold fronts during EP winters. Upper level in this section is specified as 250 hPa. Upper level troughs

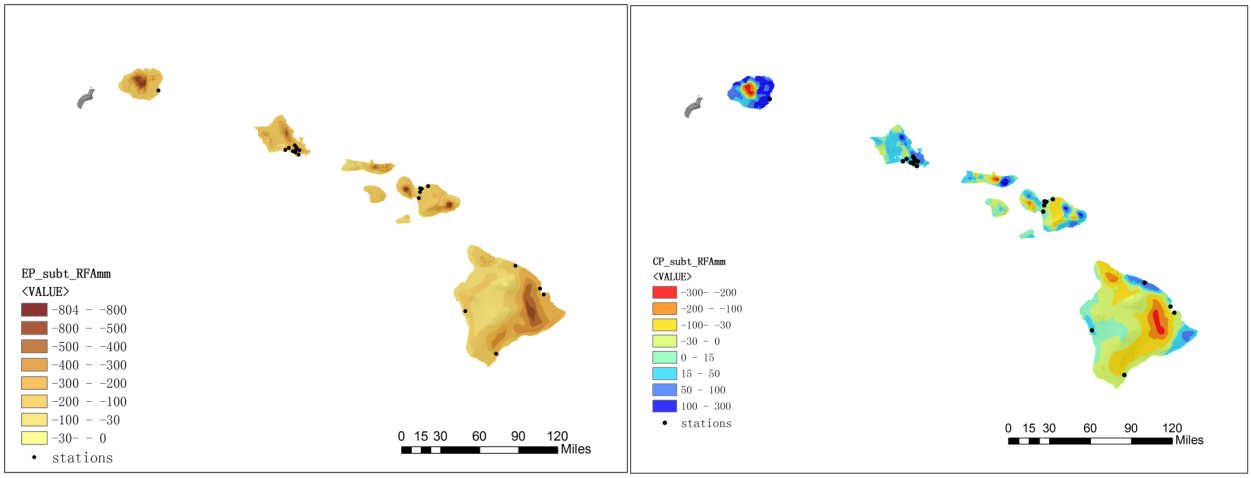

(a) EP-Climatology (b) CP-Climatology

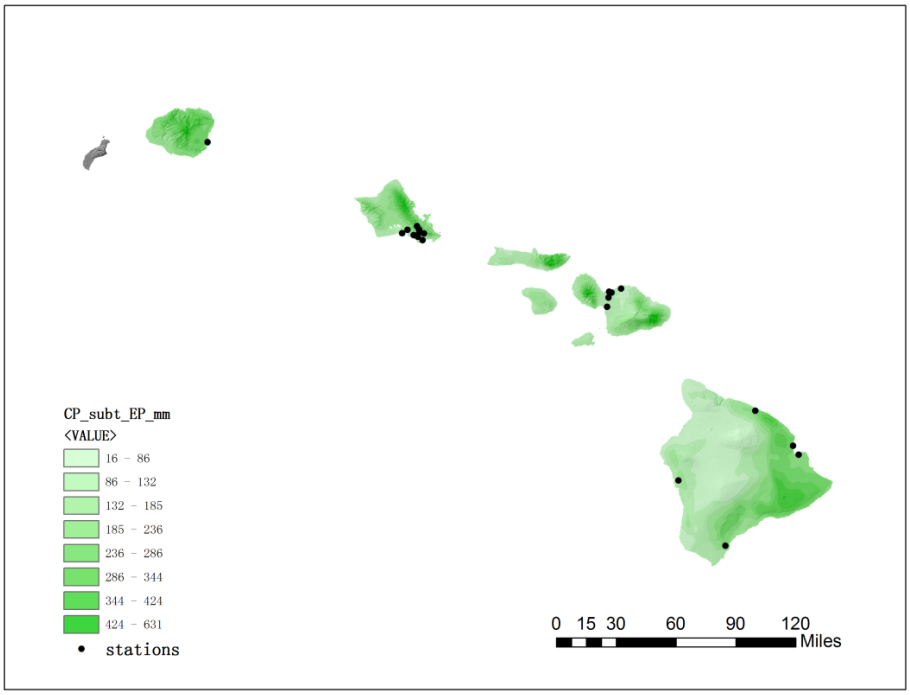

(c) CP-EP

Figure 5.11: Rainfall distribution of Hawaiian Rainfall Atlas. (a) is for EP winter anomalies, (b) is for CP winter anomalies and (c) is CP winter rainfall minus EP winter rainfall. Black dots are where the 21 stations are located.

Table 5.4: Summary of EP winter synoptic systems (upper level trough, upper level low, Kona low and cold fronts). Winter is defined as December through February.

EP events	Upper level trough	Upper level low	Kona low	Cold front
1957-58	2	1	0	6
1965-66	4	1	1	2
1972-73	3	3	0	5
1976-77	3	1	1	0
1982-83	4	0	0	2
1986-87	5	0	0	2
1991-92	2	0	0	1
1997-98	2	0	0	0
2006-07	3	1	1	5
2015-16	2	1	0	6
Average	3	0.8	0.3	2.9

are considered when the trough is south of 25° N and is east of 170° W but west of Hawaiian Islands. Upper level lows are defined as an upper level low with its center passed south of 30°N for at least 24 hours but without a surface low at the 1000 hPa level. Kona lows are defined as: (1) a closed low at upper level (250 hPa) with its center passed 30° N and last at least 24 hours; (2) a closed low at surface (1000 hPa) also with its center passed 30° N. Cold fronts are considered when the front passes at least Oahu. There are few shear lines occur during the episodes and they are counted as fronts since they are devolved from stationary fronts. From the table one can see that upper level troughs and cold fronts occur more often than upper level lows and Kona lows: 3 upper level troughs per event, 2.9 cold fronts per event, 0.8 upper level low per event and 0.3 Kona low per event.

For CP winters, as shown in Table 5.5, the frequencies of these synoptic systems are: (1) 1.63 upper level troughs per event; (2) 0.13 upper level low per event; (3) 0.5 Kona low per event and (4) 6.88 cold fronts per event. Although the average occurrence of upper level lows is 0.13, it needs to be noticed that there is only one upper level low during eight CP El Niño events. Upper level troughs and cold fronts still occur more often than upper level lows and Kona lows.

The comparison of the synoptic systems between CP and EP winters is shown in Table 5.6. The Wilcoxon-Mann-Whitney rank-sum test is applied for the data samples to test whether the synoptic system counts are significantly different during these two types of El Niño. The results show that, except for Kona lows, all the other three synoptic systems (upper level

Table 5.5: Summary of CP winter synoptic systems (upper level trough, upper level low, Kona low and cold fronts). Winter is defined as December through February.

CP events	Upper level trough	Upper level low	Kona low	Cold front
1968-69	1	0	1	7
1969-70	1	0	0	9
1987-88	1	0	2	1
1992-93	3	1	0	5
1994-95	0	0	0	4
2002-03	2	0	0	10
2004-05	3	0	1	3
2009-10	3	0	0	16
Average	1.63	0.13	0.5	6.88

Table 5.6: Synoptic systems comparison between CP and EP El Niño winters. Winter is defined as December through February.

Comparison	Upper level trough	Upper level low	Kona low	Cold front
CP-EP	-1.37	-0.67	0.2	3.98
CP/EP	0.54	0.16	1.67	2.37
(CP-EP)/EP	-46%	-84%	67%	137%

troughs, upper level lows and cold fronts) pass the 90% significance level. Although the difference of Kona lows occurrence during CP and EP winter doesn't pass the 90% significance test, the frequency of Kona lows occurrence increases 67% during CP winters compared to EP. Since Kona lows have extended life time (around 5 days) that can bring abundant rainfall to the Islands (Caruso and Businger 2006), considerable changes on Kona lows frequencies should also be considered. Also note that the frequency of cold fronts increases by 137% during CP winters as compared to EP winters. Upper level troughs and upper level lows decrease 46% and 84% during CP winters, respectively. Both Kona lows and cold fronts can change the easterly and northeasterly trade wind directions into southwesterlies. The analysis in this section could possibly explain why the lower level wind anomalies are southwesterlies when CP winters are compared to EP winters (for example, figure 5.2d and figure 5.3).

CHAPTER 6
SUMMARY AND DISCUSSION

The conclusion can be made that for the Hawaiian winter rainfall variability during EP and CP types of El Niño, the Hawaii Islands are wetter during CP winters than EP winters. During EP winters, Hawaiian Islands are drier state wide than the winter climatology. During CP winters, rainfall anomalies vary from area to area. In general, comparing to climatology, CP winters are wetter in lowlands and drier on high mountains.

This study provides new findings that the conclusions made by the previous studies on the relationship between El Niño and Hawaiian winter rainfall are more like the relationship between EP El Niño and Hawaiian winter rainfall. The relationship between CP El Niño and Hawaiian winter rainfall varies from area to area and needs more study.

The hypothesis of this study on the positive CP minus EP winter rainfall anomalies is that the lower level southwesterly wind anomalies, positive specific humidity anomalies, together with weaker descending motion over Hawaiian islands cause the relatively wetter CP winters. Further analysis on synoptic systems show that as compared to EP events, CP winters have 67 % more Kona lows and 137 % more cold fronts. The synoptic systems analysis provides the further support on this hypothesis especially on the lower level southwesterly wind anomalies factor.

The future work will be on the relationship between CP El Niño events and Hawaiian winter rainfall and will be on the WRF rainfall simulation.

APPENDIX A
INTERPOLATION METHODS

A.1 Linear Interpolation

For two known points (x_0,y_0) and (x_1,y_1), the linear interpolant is the straight line between these two points. So suppose the interpolation point (x, y) lies in between these two points:

$$y = y_0 + (x - x_0)\frac{y_1 - y_0}{x_1 - x_0}. \tag{A.1}$$

For a data set, linear interpolation is defined as the concatenation of linear interpolants between each pair of data points.

A.2 Piecewise Cubic Hermite Interpolation

Let h_k represent the length of the kth sub-interval:

$$h_k = x_{k+1} - x_k. \tag{A.2}$$

Then give the first divided difference as

$$\delta_k = \frac{y_{k+1} - y_k}{h_k}. \tag{A.3}$$

Let d_k denote the slope of the interpolant at x_k:

$$d_k = P'(x_k). \tag{A.4}$$

Considering $x_k \leq x \leq x_{k+1}$, for local variables s=x-x_k and h=h_k:

$$P(x) = \frac{3hs^2 - 2s^3}{h^3}y_{k+1} + \frac{h^3 - 3hs^2 + 2s^3}{h^3}y_k + \frac{s^2(s-h)}{h^2}d_{k+1} + \frac{s(s-h)^2}{h^2}d_k. \tag{A.5}$$

This is a cubic polynomial in s and x that satisfies four interpolation conditions, two on function values and the other two on the possibly unknown derivative values:

$$\begin{aligned} P(x_k) = y_k, P(x_{k+1}) = y_{k+1}, \\ P'(x_k) = d_k, P'(x_{k+1}) = d_{k+1}. \end{aligned} \tag{A.6}$$

Functions that satisfy interpolation conditions on derivative are known as Hermite interpolants.

To define the slopes d_k, we choose two ways in this study which are called pchip and spline in MATLAB.

A.2.1 Shape-Preserving Piecewise Cubic (pchip)

The key idea is to establish the slops d_k that the function values at least locally do not overshoot the data values. For the pchip method, if δ_k and δ_{k+1} have opposite signs or if either of them is zero then x_k can be considered as a local minimum or maximum so we can set

$$d_k = 0. \tag{A.7}$$

If δ_k and δ_{k+1} have same sign and the two intervals have the same length, then d_k is the harmonic mean of the two discrete slopes:

$$\frac{1}{d_k} = \frac{1}{2}(\frac{1}{\delta_{k-1}} + \frac{1}{\delta_k}). \tag{A.8}$$

If the two intervals have different lengths, then d_k is a weighted harmonic mean:

$$\frac{w_1 + w_2}{d_k} = \frac{w_1}{\delta_{k-1}} + \frac{w_2}{\delta_k}. \tag{A.9}$$

where $w_1=2h_k+h_k-1$, $w_2 =h_k+2h_k-1$.

A.2.2 Spline Interpolation

The first derivative P'(x) is defined by different formulas on either side of a knot x_k. Since at the knots, both formulas give the same d_k, P'(x) is continuous. In this case, on the kth subinterval, the second derivative is a linear function of $s=x-x_k$:

$$P''(x) = \frac{(6h - 12s) + (6s - 2h)d_{k+1} + (6s - 4h)d_k}{h^2}. \tag{A.10}$$

Then we can get

$$h_k d_{k-1} + 2(h_{k-1} + h_k)d_k + h_{k-1}d_{k+1} = 3(h_k\delta_{k-1} + h_{k-1}\delta_k). \tag{A.11}$$

BIBLIOGRAPHY

Ashok, K., S. K. Behera, S. A. Rao, H. Weng, and T. Yamagata, 2007: El Niño Modoki and its possible teleconnection. *J. Geophys. Res.*, **112**, C11 007, doi:10.1029/2006JC003798.

Cao, G., T. W. Gianbelluca, D. E. Stevens, and T. A. Schroeder, 2007: Inversion variability in the Hawaiian trade wind regime. *J. Climate*, **20**, 1145–1160.

Caruso, S. J. and S. Businger, 2006: Subtropical cyclogenesis over the central north pacific. *Wea. Forcasting*, **21**, 193–205.

Chen, F. and J. Dudhia, 2001: Coupling an advanced land-surface/hydrology model with the Penn State/NCAR MM5 modeling system. Part I: Model descripition and implementation. *Mon. Wea. Rev.*, **129**, 569–585.

Chu, P.-S., 1995: Hawaii rainfall anomalies and El Niño. *J. Climate*, **8**, 1697–1703, doi: 10.1175/1520-0442(1995)008⟨1697:HRAAEN⟩2.0.CO:2.

Chu, P.-S. and H. Chen, 2005: Interannual and interdecadal rainfall variations in the Hawaiian Islands. *J. Climate*, **18**, 4796–4813.

Chu, P.-S., A. J. Nash, and F.-Y. Porter, 1993: Diagnostic studies of two contrasting rainfall episodes in Hawaii: Dry 1981 and wet 1982. *J. Climate*, **6**, 1457–1462.

Collins, W. D. and Coauthors, 2004: Descripition of the NCAR Community Atmosphere Model (CAM3.0). Note, NCAR Tech.

Dee, D. P. and Coauthors, 2011: The ERA-Interim reanalysis: Configuration and performance of the data assimilation system. *Quart. J. Roy. Meteor. Soc.*, **137**, 553–597.

Diaz, H. F. and T. W. Giambelluca, 2012: Changes in atmospheric circulation patterns associated with high and low rainfall regimes in the Hawaiian islands region on multiple time scales. *Global and Planetary Change*, **98-99**, 97–108.

Giambelluca, T. W., Q. Chen, A. G. Frazier, J. P. Price, Y.-L. Chen, P.-S. Chu, J. K. Eischeid, and D. M. Delparte, 2013: Online rainfall atlas of Hawaii. *Bull. Amer. Meteor. Soc.*, **94**, 313–316, doi:10.1175/BAMS-D-11-00228.1.

Held, I. M. and A. Y. Hou, 1980: Nonlinear axially symmetric circulations in a nearly inviscid Atmosphere. *J. Atmospheric Sciences*, **37**, 515–533.

Hong, S.-Y. and J. Lim, 2006: The WRF single-monent 6-class microphysics scheme (wsm6). *J. Korean Meteor. Soc.*, **42**, 129–151.

Hong, S.-Y., Y. Noh, and J. Dudhia, 2006: A new vertical diffusion package with an explicit treatment of entrainment processes. *Mon. Wea. Rev.*, **134**, 2318–2341.

Huang, B., et al., 2015: Extended reconstructed sea surface temperature (ERSST), Version 4: Part I. Upgrades and intercomparisons. *J. Climate*, **28**, 911–930, doi:10.1175/JCLI-D-14-00006.1.

Kalnay and Coauthors, 1996: The NCEP/NCAR 40-year reanalysis project. *Bull. Amer. Meteor. Soc.*, **77**, 437–470.

Kao, H.-Y. and J.-Y. Yu, 2009: Contrasting eastern-Pacific and central-Pacific types of El Niño. *J. Climate*, **22**, 615–632, doi:10.1175/2008JCLI2309.1.

Kug, J., F.-F. Jin, and S.-I. An, 2009: Two types of El Niño events: cold tongue El Niño and warm pool El Niño. *J. Climate*, **22**, 1499–1515, doi:10.1171/2008JCLI2624.1.

Larkin, N. K. and D. E. Harrison, 2005a: Global seasonal temperature and precipitation anomalies during El Niño autumn and winter. *Geophys. Res. Lett.*, **32**, L16 705, doi:10.1029/2005GL022860.

Larkin, N. K. and D. E. Harrison, 2005b: On the definition of El Niño and associated seasonal average U.S. weather anomalies. *Geophys. Res. Lett.*, **32**, L16 705, doi:10.1029/2005GL022738.

Lawrimore, J., 2016: Global summary of the month, version 1.0. doi:10.7289/V5QV3JJ5.

Lee, T. and M. J. McPhaden, 2010: Increasing intensity of El Niño in the central-equatorial Pacific. *Geophys. Res. Lett.*, **37**, L14 603, doi:10.1029/2010GL044007.

Leopold, L. B., 1951: Hawaiian climate: its relation to Human and plant geography. *Meteor. Monogr.*, **1, No. 3**, 1–6.

Leung, L. R., Y. H. Kuo, and J. Tribbia, 2006: Research needs and directions of regional climate modeling using WRF and CCSM. *Amer. Meteror. Soc.*, **87**, 1747–1751.

Lyons, S. W., 1982: Empirical orthogonal function analysis of Hawaiian rainfall. *J. Appl. Meteor.*, **21**, 1713–1729.

Morrison, I. and S. Businger, 2001: Synoptic structure and evolution of a Kona low. *Wea. Forecasting*, **16**, 81–98.

O'Connor, C. F., P.-S. Chu, P.-C. Hsu, and K. Kodama, 2015: Variability of Hawaiian winter rainfall during La Niña events since 1956. *J. Climate*, **28**, 7809–7823.

Ren, H.-L. and F.-F. Jin, 2011: Niño indices for two types of ENSO. *Geophys. Res. Lett.*, **38**, L04 704, doi:10.1029/2010GL046031.

Skamarock, W. C., J. B. Klemp, J. Dudhia, D. O. Gill, D. M. Barker, W. Wang, and J. G. Powers, 2008: A description of the Advanced Research WRF version 3. Note, NCAR Tech.

Takahashi, K., A. Montecinos, K. Goubanova, and B. Dewitte, 2011: Reinterpreting the canonical and Modoki El Niño. *Geophys. Res. Lett*, **38**, L10 704, doi:10.1029/2011GL047364.

Timm, O. and H. F. Diaz, 2009: Synopitic-statistical approch to regional downscaling of IPCC twenty-first-centrary climate projections: Seasonal rainfall over the Hawaiian Islands. *J. Climate*, **22**, 4216–4280, doi:10.1175/2009JCLI2833.1.

Wang, Y., O. L. Sen, and B. Wang, 2003: A highly resolved regional climate model (IPRC_RegCM) and its simulation of the 1998 severe precipitation events over China. Part I: Model description and verification of simulation. *J. Climate*, **16**, 1721–1738.

Wang, Y., S.-P. Xie, H. Xu, and B. Wang, 2004: Regional model simulations of marine boundary layer clouds over the Southeast Pacific off South America. Part I: Control experiment. *Mon. Wea. Rev.*, **132**, 274–296.

Wilks, D. S., 2011: *Statistical methods in the Atmospheric Sciences*, International Geophysics Series, Vol. 100. 3d ed., Academic Press, 676 pp.

Wyrtki, K. and G. Meyers, 1976: The trade wind field over the Pacific Ocean. *J. Appl. Meteor.*, **15**, 698–704, doi:10.1175/1520-0450(1976)015⟨0698:TTWFOT⟩2.0.CO;2.

Zhang, C.-X., Y. Wang, A. Lauer, and K. Hamilton, 2012: Configuration and evaluation of the wrf model for the study of Hawaiian regional climate. *Mon. Wea. Rev.*, **140**, 3259–3277.

Zhang, Y., V. Dulière, P. W. Mote, and E. P. Salethé, 2009: Evaluation of WRF and HadRM mesoscale climate simulations over the U.S. Pacific Northwest. *J. Climate*, **22**, 5511–5526.